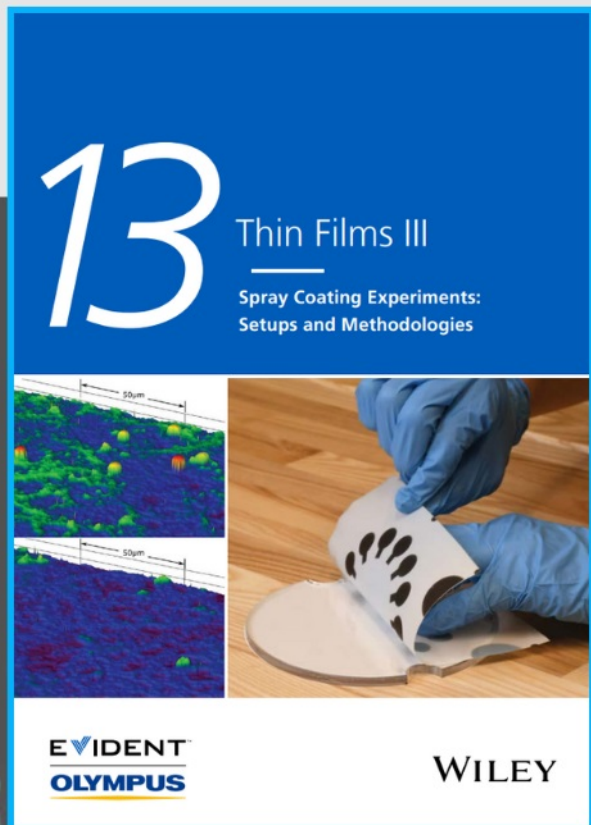




# Spray Coating Experiments: Setups and Methodologies

**The latest eBook from  
Advanced Optical Metrology.  
Download for free.**



*Spray Coating Experiments: Setups and Methodologies*, is the third in our Thin Films eBook series. This publication provides an introduction to spray coating, three article digests from Wiley Online Library and the latest news about Evident's Image of the Year Award 2022.

Wiley in collaboration with Evident, are committed to bridging the gap between fundamental research and industrial applications in the field of optical metrology. We strive to do this by collecting and organizing existing information, making it more accessible and useful for researchers and practitioners alike.

**EVIDENT**  
**OLYMPUS**

**WILEY**

# Entrapped Molecule-Like Europium-Oxide Clusters in Zinc Oxide with Nearly Unaffected Host Structure

Soham Mukherjee,\* Sarmad Naim Katea, Emille M. Rodrigues, Carlo. U. Segre, Eva Hemmer, Peter Broqvist, Håkan Rensmo,\* and Gunnar Westin\*

Nanocrystalline ZnO sponges doped with 5 mol%  $\text{Eu}_{1.5}\text{O}_{1.5}$  are obtained by heating metal–salt complex based precursor pastes at 200–900 °C for 3 min. X-ray diffraction, transmission electron microscopy, and extended X-ray absorption fine structure (EXAFS) show that phase separation into ZnO:Eu and  $\epsilon\text{-Eu}_2\text{O}_3$  takes place upon heating at 700 °C or higher. The unit cell of the clean oxide made at 600 °C shows only  $\approx 0.4\%$  volume increase versus undoped ZnO, and EXAFS shows a ZnO local structure that is little affected by the Eu-doping and an average  $\text{Eu}^{3+}$  ion coordination number of  $\approx 5.2$ . Comparisons of 23 density functional theory-generated structures having differently sized Eu-oxide clusters embedded in ZnO identify three structures with four or eight Eu atoms as the most energetically favorable. These clusters exhibit the smallest volume increase compared to undoped ZnO and Eu coordination numbers of 5.2–5.5, all in excellent agreement with experimental data. ZnO defect states are crucial for efficient  $\text{Eu}^{3+}$  excitation, while  $\epsilon\text{-Eu}_2\text{O}_3$  phase separation results in loss of the characteristic  $\text{Eu}^{3+}$  photoluminescence. The formation of molecule-like Eu-oxide clusters, entrapped in ZnO, proposed here, may help in understanding the nature of the unexpected high doping levels of lanthanide ions in ZnO that occur virtually without significant change in ZnO unit cell dimensions.

ions to optimize the electronic structure or to endow ZnO with additional optical, magnetic or catalytic properties has been extensively investigated. However, in spite of an immense research effort over the last two decades, there is still a large variety in the results reported on the properties of similarly doped ZnO structures, some of which are even contradictory. This may to a great degree be related to differences in crystal quality, grain boundaries, and perhaps most importantly, the doping structure, i.e., the spatial distribution and local coordination of the dopant ions in the host structure.<sup>[38–41]</sup> In spite of this, there are few studies that describe the dopant structure in sufficient detail to connect the properties with the actual structure. As a further complication, the structure and chemical contents vary with synthesis technique and heat-treatment, which thus have a profound effect on the optical and magnetic properties, as well as on the electronic band-structure. A recent illustrative example is the research

on Co-doped ZnO aiming for diluted magnetic semiconductors (DMS) that, based on theoretical results, shows promise for room-temperature spin-polarized electron transport, with potential to revolutionize the electronics industry.<sup>[17,18,42]</sup> In this area, the large number of reports yields a scattered picture of the magnetic properties, and sometimes completely contradictory results. When investigating the materials in detail, it was

## 1. Introduction

ZnO-based semiconductors have gained enormous interest due to their potential for use in solar cells,<sup>[1–11]</sup> photocatalysts,<sup>[12–16]</sup> diluted magnetic semiconductors,<sup>[17–20]</sup> piezoelectric generators,<sup>[1–3]</sup> sensors,<sup>[1,3,21–27]</sup> optoelectronics,<sup>[1,2,26,27]</sup> green fuel catalysts,<sup>[28–33]</sup> and energy storage.<sup>[4,34–37]</sup> Doping with metal

S. Mukherjee, H. Rensmo  
Department of Physics and Astronomy  
Ångström Laboratory  
Uppsala University  
Uppsala 75237, Sweden  
E-mail: soham.mukherjee@physics.uu.se; hakan.rensmo@physics.uu.se

 The ORCID identification number(s) for the author(s) of this article can be found under <https://doi.org/10.1002/smll.202203331>.

© 2022 The Authors. Small published by Wiley-VCH GmbH. This is an open access article under the terms of the Creative Commons Attribution License, which permits use, distribution and reproduction in any medium, provided the original work is properly cited.

<sup>[†]</sup>Present address: Höganäs AB, Bruksgatan 35 – SE 26383, Sweden

S. N. Katea,<sup>[†]</sup> P. Broqvist, G. Westin  
Department of Chemistry-Ångström  
Ångström Laboratory  
Uppsala University  
Uppsala 75121, Sweden  
E-mail: gunnar.westin@kemi.uu.se

E. M. Rodrigues, E. Hemmer  
Department of Chemistry and Biomolecular Sciences  
University of Ottawa  
Ottawa, Ontario K1N 6N5, Canada  
Carlo. U. Segre  
Center for Synchrotron Radiation Research and Instrumentation and  
Department of Physics  
Illinois Institute of Technology  
Chicago, IL 60616, USA

DOI: 10.1002/smll.202203331



shown that the differences mainly depended on the cobalt oxidation state, including local formation of the  $(\text{Zn},\text{Co})_3\text{O}_4$  spinel phase, and clustering of  $\text{Co}^{2+}$  ions residing at  $\text{Zn}^{2+}$  ion positions, resulting in a paramagnetic response from peripheral cobalt ions.<sup>[43–52]</sup> This is a general finding applicable also to other oxide semiconductors that strongly hampers the progress of, e.g., solar hydrogen catalysts. For example, Ti-doped  $\alpha\text{-Fe}_2\text{O}_3$  shows very different properties depending on synthesis techniques, in the whole range from improving the photo-catalytic activity to reducing it.<sup>[53]</sup>

Lanthanide (Ln)-doped semiconductors, including ZnO, have gained interest as potential photocatalysts or optoelectronic devices, where the most studied system is Eu-doped ZnO.<sup>[54–56]</sup> Some of the materials reported contain unexpected high doping levels of 5% Eu and higher, when considering the much larger ionic radius and aliovalency of  $\text{Eu}^{3+}$  ions, compared to the  $\text{Zn}^{2+}$  ions of the host structure. Therefore, there has been an ongoing discussion on the reality and nature of such Eu-doped ZnO, not the least due the close-to-zero changes in X-ray diffraction (XRD) derived unit cell dimensions that were observed even at high levels of Eu-doping. A short review focused on the synthesis and connected structural properties is given in the in the supporting material in ref. <sup>[57]</sup>, while other reviews provide a more general overview on Ln-doped ZnO and their properties.<sup>[54,56]</sup> It has recently been proven beyond doubt, that the Eu ions may be completely situated within the ZnO crystals of the nanocrystalline Eu-doped ZnO sponges synthesized at temperatures below 700 °C.<sup>[57,58]</sup> In these studies, thermogravimetric (TG) analysis, XRD, X-ray photoelectron spectroscopy (XPS), IR spectroscopy, scanning electron microscopy (SEM), transmission electron microscopy (TEM)-electron diffraction (ED)/energy dispersive X-ray spectroscopy (EDS), scanning transmission electron microscopy (STEM)-electron energy loss spectroscopy (EELS) mapping, and optical measurements were used to describe the chemistry and structure. It was shown that the Eu ions resided within the ZnO crystals without any visible phase separation from TEM imaging or XRD analysis, but their local dopant structure remained unknown. Therefore, in this work, to be able to understand how large amounts of the big  $\text{Eu}^{3+}$  ions may be introduced into the ZnO phase without changing the ZnO unit cell volume, a more detailed study on 5%Eu-doped ZnO was conducted using extended X-ray absorption fine structure (EXAFS). This technique allowed a revelation of the local  $\text{Eu}^{3+}$ - and  $\text{Zn}^{2+}$ -ion coordination numbers, bond lengths, and types of neighboring atoms. Experimental data were compared with density functional theory (DFT)-generated structures based on ZnO with dopant ions embedded as  $\text{Eu}^{3+}$  ion pairs replacing three  $\text{Zn}^{2+}$  ions thereby forming one  $\text{Zn}^{2+}$  vacancy. Clusters of up to eight Eu ions were studied. The Eu-ion coordination number (CN), Eu–Eu distances, ZnO cell volume, and formation energies were calculated. The obtained values were compared to experimental data derived from EXAFS and the very small unit-cell volume expansion in 5%Eu-doped ZnO obtained from XRD, as compared with pure ZnO. A very good agreement between the theoretical and experimental data was found for three clusters built by four or eight Eu ions. This allows for the understanding of the unexpected doping structure and how the ZnO unit cell dimensions can be retained on doping with high levels of large, aliovalent

ions such as  $\text{Eu}^{3+}$ . Furthermore, the changes in coordination over the temperature range 200–900 °C were examined in order to follow the effects of Eu doping. The lowest synthesis temperature of 200 °C yielded slightly impure samples, while clean Eu-doped ZnO was obtained at 600 °C. In a temperature range of 700–900 °C, some Eu were expelled from the ZnO crystals yielding 5–10 nm sized  $\text{c-Eu}_2\text{O}_3$  particles on the ZnO sponge surface. The Eu-doped ZnO microstructures were also explained from SEM and TEM imaging, although more thorough microscopy studies, including TEM-EELS mapping, have been provided elsewhere.<sup>[57,58]</sup> Photoluminescence spectroscopy provided additional insight into the defect structure of ZnO sponges as well as the effect of Eu-clustering and  $\text{c-Eu}_2\text{O}_3$  phase separation on the characteristic  $\text{Eu}^{3+}$  emission.

Based on the results obtained in this study, highly complex and hitherto unforeseen molecule-like dopant structures are proposed that may shed light on various structural, magnetic, and optical data for this kind of semiconductor materials, otherwise hard to explain. The findings reported herein also point toward a general possibility to form clusters of “misfit”-ions accommodated in rigid semiconductor structures. These concepts may be used for the design of optical, magnetic, catalytic, and transport properties, where typically a high dopant level is desired, since semiconductor properties are sensitive to structural disturbances.

## 2. Experimental Section

### 2.1. Chemicals and Synthesis

All chemicals were used as received. The actual molecular weights of the hydrated salts were determined gravimetrically as  $\text{Eu}_2\text{O}_3$  and ZnO, respectively. Nanocrystalline sponges of ZnO and ZnO with 5 mol%  $\text{EuO}_{1.5}$  in ZnO (ZnO:5%Eu) were synthesized as previously reported.<sup>[57]</sup> Briefly, zinc dinitrate hexahydrate ( $\text{Zn}(\text{NO}_3)_2 \cdot 6\text{H}_2\text{O}$ , Sigma-Aldrich >99%), zinc diacetate dihydrate ( $\text{Zn}(\text{OAc})_2 \cdot 2\text{H}_2\text{O}$ , Sigma-Aldrich >99%), and triethanolamine (TEA, Sigma-Aldrich p.a.) in methanol (Scharlau, analytical grade 99.9%) were mixed with appropriate amounts of europium trinitrate pentahydrate ( $\text{Eu}(\text{NO}_3)_3 \cdot 5\text{H}_2\text{O}$ , Aldrich 99.9%) and triethanolamine (TEA) in methanol. Then, the solution was evaporated to a transparent or whitish paste on a Petri-dish and heated for 3 min in a muffle furnace kept at 200, 300, 400, 500, 600, 700, 800, or 900 °C. Upon heating at 200 °C or higher temperatures, a very light, voluminous ZnO or ZnO:Eu sponge powder was formed. Thus, some kind of structure containing the powder is recommended.

### 2.2. Sponge Microstructure from XRD, SEM, and TEM

The pure and Eu-doped ZnO, obtained by heating the precursor paste for 3 min at temperatures from 200 to 900 °C, were studied with powder X-ray diffraction (PXRD) in  $\theta$ - $2\theta$  mode using Cu  $K\alpha$  radiation in a Bruker D8 Advance instrument equipped with an Ni filter. The crystalline phases, unit-cell parameters, and crystal sizes were determined with the Topas software. The cif-files used were obtained from PDF Card

00-036-1451 (hexagonal ZnO, space group  $P6_3mc$ ) and PDF Card 00-034-0392 (cubic  $\text{Eu}_2\text{O}_3$ , space group  $Ia3$ ). The overall microstructure of the sponges was studied with a Zeiss Merlin field-emission gun SEM, while the detailed microstructure was studied with a JEOL 2100F TEM operated at 200 kV.

### 2.3. Local Structure from EXAFS

EXAFS measurements were performed at the Materials Research Collaborative Access Team (MRCAT) bending-magnet beamline (Sector 10) at Argonne National Laboratory's Advanced Photon Source. This beamline uses a water-cooled Si (111) double crystal monochromator and collimating slits for energy selection and optimal energy resolution. EXAFS measurements were performed in transmission mode at the Zn  $K$  and Eu  $L_3$  edges on ZnO:5%Eu sponges prepared at 200, 600, 700, 800, and 900 °C. The sample amount was adjusted to yield a total absorption coefficient ( $\mu x$ ) of around 2.5 after the edge in order to ensure a linear response. Measured quantities of powdered sample, amounting to  $\approx 40$  mg, were thoroughly mixed with boron nitride and pressed into 10 mm diameter pellets and mounted in Kapton tape for EXAFS measurements. A Zn foil was measured as reference to track any energy shift between the scans. The reference energies obtained were used for edge energy alignment during the data processing.  $\text{Eu}_2\text{O}_3$  was used as Eu reference material, while the elemental reference was calibrated using an Fe foil. Each scan was taken with a step of 5 eV in the pre-edge region, 0.2 eV in the XANES ( $-50$  to  $+50$  eV) region and 2 eV for the rest of the scan. The EXAFS data were analyzed by the IFEFFIT interactive XAFS data analysis package using AUTOBK for background subtraction and the FEFF8 software for calculating theoretical scattering amplitudes and phases for a pair of atoms, using the input file prepared by the ATOMS program that uses the standard crystallographic data. For each measured X-ray absorption spectrum, the EXAFS signal  $\chi(k)$  was extracted using AUTOBK.  $\chi(k)$  is generally defined as

$$\chi(k) = \sum_j \frac{N_j S_0^2 f_j(k) e^{-2R_j/\delta_j(k)} e^{-2k^2\sigma_j^2}}{k R_j^2} \sin[2kR_j + \delta_j(k)] \quad (1)$$

where  $k$  is the photoelectron wavenumber;  $f_j(k)$  and  $\delta_j(k)$  represent the photoelectron back-scattering amplitude and phase shift, respectively, for the  $j$ th shell;  $\lambda_j(k)$  is the photoelectron inelastic mean free path;  $N_j$ ,  $R_j$ , and  $\sigma_j^2$  represent the CN, interatomic distance, and mean-square disorder in  $R_j$  ( $j$ th coordination shell); and  $S_0^2$  is the amplitude reduction factor. The XAS data were first converted to absorption versus energy scale, followed by energy calibration against respective metal foils, pre-edge background removal using a linear fit, and post-edge background removal using a third-order polynomial. Multiple scans (three scans for Zn  $K$  and 7–10 scans for Eu  $L_3$  edge per sample with no identifiable beam damage) for each edge were then properly aligned, merged to get significant statistics and eventually normalized to have an edge step of 1 using the Athena software. The background below  $R_{bkg} = 1.0$  Å was minimized by using the built-in AUTOBK algorithm. The final merged scans for each

metal edge were simultaneously analyzed, using the theoretical fitting standards computed with the FEFF6 software. Input for FEFF was prepared using the ATOMS program and the crystallographic data. The data were analyzed using FEFFIT software.

### 2.4. Modeling by DFT

The electronic structure calculations performed in this work were based on DFT in the implementation with plane waves and pseudopotentials. The exchange-correlation energy contribution to the total energy was modeled using the approximation proposed by Perdew–Burke–Ernzerhof (PBE).<sup>[59,60]</sup> Projector augmented wave (PAW) pseudopotentials,<sup>[61,62]</sup> describing explicitly 6, 12, and 9 electrons, were used for O( $2s^2p^4$ ), Zn( $3d^{10}4s^2$ ), and Eu( $5d^1p^62s^2$ ), respectively. For Eu, the chosen pseudopotential was earlier used to accurately describe the  $\text{Eu}^{3+}$  oxidation state. In the current investigation of Eu-dopants in ZnO, explicit effects of spin polarization in the  $\text{Eu}^{3+}$  ions were not accounted for. All calculations were performed using the Vienna Ab Initio Simulation Package (VASP).<sup>[63–66]</sup>

The bulk ZnO host was modeled using an orthorhombic representation of the hexagonal ZnO as basis, with a unit cell of  $9.86 \times 10.60 \times 11.38$  Å<sup>3</sup>, containing in total 48 ZnO units, as obtained from the cell optimization at the current level of theory. Upon Eu-doping, this unit cell, and repetitions of it, to keep a doping concentration of 4.25 mol%  $\text{EuO}_{1.5}$  (2 Eu + 45 Zn + 1 vacancy + 48 O) were used. The cut-off energy, truncating the plane-wave basis set, was set to 600 eV, and the  $k$ -point sampling of the Brillouin zone was kept at correspondingly a  $3 \times 3 \times 3$   $k$ -point sampling, using the Monkhorst–Pack scheme, for the smallest unit cell. Optimization of both metal positions and cell volumes was performed for all structures presented until the largest force on each atom was smaller than 0.001 eV/atom. Along with total energy evaluations, the radial distribution functions—partial and full—were computed to allow for comparisons with the distances and coordination numbers, as obtained from the experimental EXAFS and XRD data.

### 2.5. Optical Properties

Excitation and emission photoluminescence spectra were obtained using a Horiba QuantaMaster 8075-21 spectrofluorometer, equipped with a double additive excitation monochromator with triple gratings, a single emission monochromator with triple gratings, and a UV–vis PMT detector (Hamamatsu PMT R928). The excitation source used for the recording of steady-state excitation and emission spectra was a 75 W continuous Xenon lamp, while a 450 W pulsed Xenon lamp was used for the time-resolved emission spectra. All samples were analyzed at room temperature, in the solid-state as pellets between 1 mm thick quartz windows using a 90° configuration between the excitation beam and emission detector. The excitation spectra were corrected in real time according to the response of the excitation monochromators and the lamp intensity. The emission spectra were corrected according to the sensitivity of the photomultiplier detector and response of the monochromator gratings.

## 2.6. Statistical Analysis

### 2.6.1. EXAFS

The number of independent parameters  $N_{idp}$  was determined by the Nyquist criterion  $\approx 2 \cdot \Delta k \cdot \Delta R / \pi$ . Fits to the Zn K and Eu L<sub>3</sub> data were obtained using theoretically calculated scattering factors from FEFF8. The program uses Levenberg–Marquardt nonlinear minimization method which essentially minimizes the  $\chi^2$  fitting metric. The  $\chi^2$  is defined as

$$\chi^2 = \frac{N_{idp}}{N} \sum_{i=1}^N \left( \frac{f_i}{\epsilon_i} \right)^2 \quad (2)$$

where  $N$  is the number of data points,  $\epsilon_i$  is the measurement uncertainty at data point  $i$ ,  $f_i$  is the difference function between the experimental and computed data at each point  $i$  used in the fit, and  $N_{idp}/N$  scales  $\chi^2$  to the number of independent data measured. The fitting metrics were determined through R-factor and reduced  $\chi^2_v$  ( $=\chi^2/v$ ) where  $v$  is the difference between  $N_{idp}$  and the number of parameters evaluated in the fit. The diagonal elements of the fitting matrix are the error limits which are scaled by  $\sqrt{\chi^2_v}$  and minimized within a margin of  $1\sigma$  uncertainties.

## 3. Results and Discussion

### 3.1. Sponge Microstructure by XRD, SEM, and TEM

The synthesis of Eu-doped sponge structures built of nanocrystallites has previously been reported in detail.<sup>[57,58,67]</sup> In the present study, ZnO and ZnO:5%Eu sponges were prepared by heating precursor pastes in air for 3 min at 200, 300, 400, 500, 600, 700, 800, and 900 °C, respectively. SEM and TEM images (Figure 1a–i) show the microstructures of the ZnO:5%Eu sponges, as obtained after heating at 200, 600, and 800 °C.

The ZnO:5%Eu sponge obtained at 200 °C contained minor amounts of organic residues, including carboxyl groups, while heating at 400 °C left only minor amounts of carbonate impurities.<sup>[57]</sup> Heating at 600 °C decomposed the carbonate, yielding a pure, Eu-doped zinc oxide sponge without any detectable phase segregation.<sup>[57,58]</sup> Heating at 700 °C led to very minor phase segregation as observed by TEM,<sup>[57]</sup> but it was not detectable by XRD (Figure 1j,k). After heating at 800 °C, *c*-Eu<sub>2</sub>O<sub>3</sub> was clearly segregated as 5–10 nm sized particles on the ZnO:Eu sponge surface, as shown by TEM and corroborated by XRD, respectively (Figure 1i–k). Phase analysis by XRD indicated that  $\approx 50\%$  and  $70\%$  of the europium was present as *c*-Eu<sub>2</sub>O<sub>3</sub> at 800 and 900 °C, respectively, while the rest remained within the ZnO host lattice.<sup>[57]</sup> TEM studies showed that the ZnO grain connectivity was intimate for the 600 and 800 °C sponges (Figure 1e,f), in contrast to that of the 200 °C sponge (Figure 1d), which showed more rounded, less tightly connected grains.

### 3.2. Local Structure of the ZnO:5%Eu Sponges by EXAFS

The element selectivity of the EXAFS technique allows the probing of the local environment of the host and dopant ions separately,

which is essential especially for obtaining the disordered Eu-dopant structure. ZnO and ZnO:5%Eu sponges prepared during 3 min at 200, 400, 600, 700, 800, and 900 °C, respectively, were studied with EXAFS, along with *c*-Eu<sub>2</sub>O<sub>3</sub> for comparison.

#### 3.2.1. Zn Environment

Figure 2a shows  $\chi(k)$  functions for the Zn K edge in the ZnO:5%Eu sponges made at 200–900 °C. The  $\chi(k)$  oscillations remained well-defined up to high photoelectron wavenumbers of  $k_{max} \approx 14.0 \text{ \AA}^{-1}$ , indicating a high degree of short-range order in the Zn environment. The major frequency components of the  $\chi(k)$  functions are similar to those of pure ZnO, suggesting that the presence of Eu did not significantly modify the local environment around Zn. Isolation of the individual frequency components of  $\chi(k)$  functions by Fourier transforming (FT) the data to the corresponding  $\chi(R)$  functions revealed a clear dampening effect with lowering of synthesis temperatures (Figure 2b), which to some extent may be related to the increasing crystallite sizes in the range 700–900 °C (see Figure 1k).

However, the amplitude dampening of the samples obtained at 200 and 600 °C stood out, being much stronger than those found for the higher temperature samples (Figure 2b), albeit the fact that these samples had rather similar ZnO crystal sizes of  $\approx 10 \text{ nm}$ . This shows that the ZnO crystal size is not the only decisive factor behind the dampening. A presence of cavities, hosting Eu-oxide clusters within the ZnO crystals, may effectively act in the same way as grain boundaries to reduce the long-range ordering (vide infra). Synthesis temperatures of 700 °C and higher are expected to reduce the amount of such cluster filled cavities as *c*-Eu<sub>2</sub>O<sub>3</sub> is expelled from the ZnO grains. It is therefore likely that the dampening of the amplitudes due to long-range order has different origins dominating at low and at high synthesis temperatures, respectively.

The peaks observed in the  $\text{mod}[\chi(R)]$  functions correspond to scattering from near neighboring (NN) atoms occurring at different distances from a central Zn ion ( $R = 0 \text{ \AA}$ ). Zn EXAFS parameters were extracted by fitting the  $\chi(R)$  data over the range 1.1–3.5 Å using a Hanning window. An overlay plot of the real part of the  $\chi(R)$  functions and their corresponding fits are shown in Figure S1a (Supporting Information). Details of the fitting procedures applied, extracted local parameters and fit quality parameters for each sample at the Zn K edge and a comparison of different models based on these parameters are provided in Table S1 (Supporting Information).

The first EXAFS peak, corresponding to the 1NN environment, indicated three short Zn–O bonds of  $1.958 \pm 0.007 \text{ \AA}$  and one slightly longer Zn–O bond of  $1.981 \pm 0.007 \text{ \AA}$  (Table S1, Supporting Information), in similarity to the *h*-ZnO structure with three shorter bonds of  $1.974 \text{ \AA}$  and one longer bond of  $1.989 \text{ \AA}$ , as determined by XRD.<sup>[57]</sup> As indicated above, the Zn 1NN (the CN of O around Zn) was slightly below four for the 200 °C sample, which seems likely as due to the smaller crystallite sizes. These crystals expose more of oxygen-poor surfaces, due to the more rounded grain shape and less intimate grain contacts (Figure 1d–f), but also carry more cavities containing Eu-oxide clusters interrupting the homogeneous ZnO crystal.



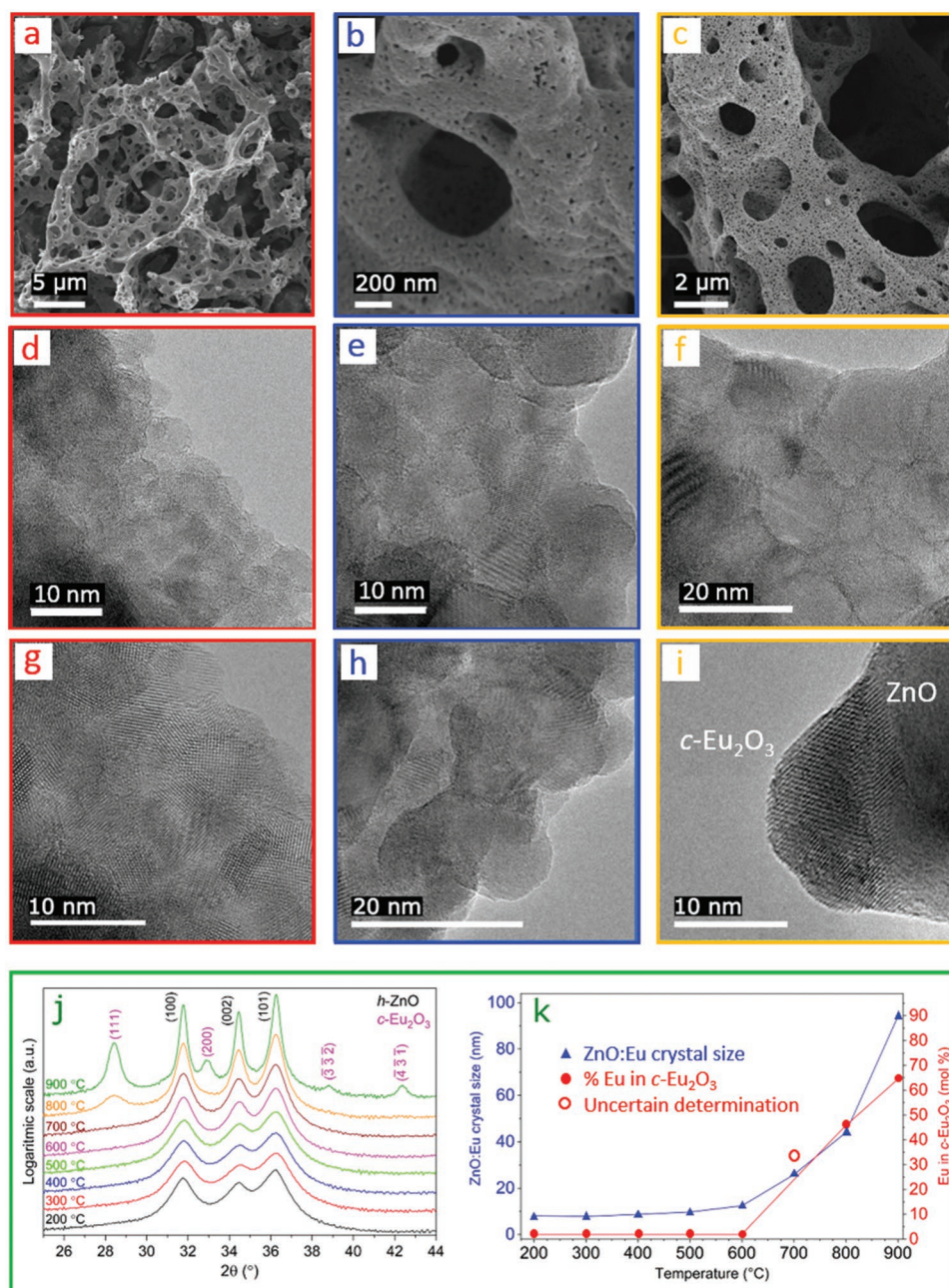


**Figure 1.** SEM and TEM images of ZnO:5%Eu sponges heated for 3 min at a,d,g) 200 °C, b,e,h) 600 °C, and c,f,i) 800 °C. j) XRD patterns for ZnO:5%Eu sponges and k) XRD-derived mole fraction of Eu present in the *c*-Eu<sub>2</sub>O<sub>3</sub> as well as ZnO crystal sizes of sponges obtained at 200, 300, 400, 500, 600, 700, 800, and 900 °C, all for 3 min.

The second EXAFS peak observed in Figure 2b includes contributions from 2NN (the Zn, Eu coordination shell) and 3NN (the next O coordination shell). The spatial distribution of 2NN (six short Zn–Zn and six long Zn–Zn interatomic distances) and 3NN (one short, six medium, and three long Zn–O approximated<sup>[68]</sup> as nine long Zn–O) are shown in Figure 2c. The CNs of Zn ( $n_{\text{Zn-Zn}}$ ), Eu ( $n_{\text{Zn-Eu}}$ ), and O atoms ( $n_{\text{Zn-O}}$ ) surrounding the Zn ions, extracted from the EXAFS analysis, are shown in Figure 2d. The sum of  $n_{\text{Zn-Zn}}$  and  $n_{\text{Zn-Eu}}$  gives the total 2NN coordination number ( $n_{2\text{NN}}$ ) around Zn.  $n_{2\text{NN}}$

values down to  $\approx 10$  were obtained for the samples made at 200–700 °C, while the samples made at higher temperatures, 800 and 900 °C, approached the ideal bulk limit value of 12 for pure *h*-ZnO (Figure 2d). Such a lowering of  $n_{2\text{NN}}$  values in case of the lower temperature samples cannot be explained merely by competing Zn–Zn and Zn–Eu interactions alone, considering the low amount of Eu present in the sponges. Instead, the lower  $n_{2\text{NN}}$  values are most likely also due to a size effect. Since Zn EXAFS provides volume-averaged local information about all Zn ions, smaller crystallite sizes that develop at lower

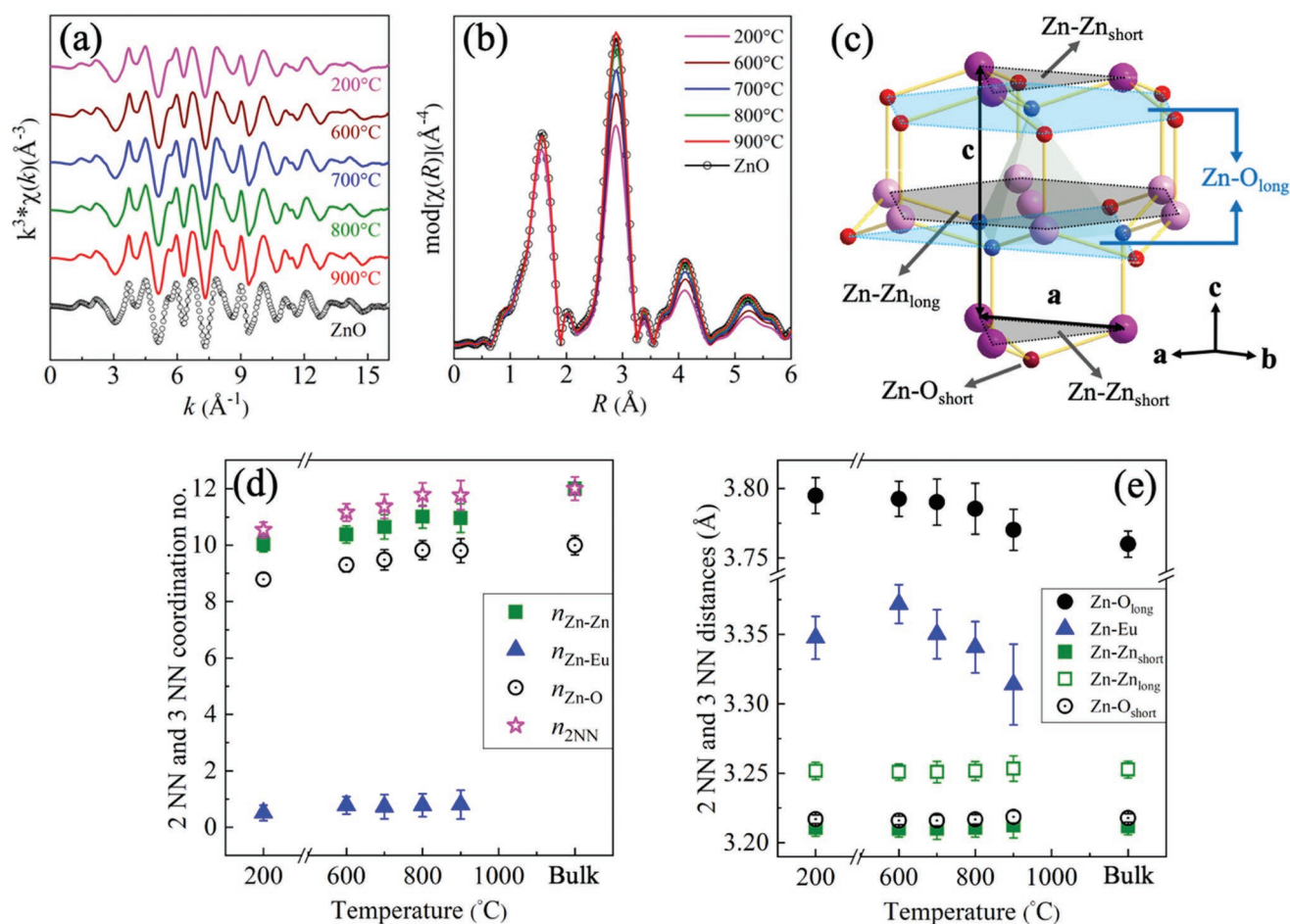


**Figure 2.** a) Zn K  $\chi(k)$  functions ZnO:5%Eu and undoped *h*-ZnO sponges synthesized at 200, 600, 700, 800, and 900 °C. b) Modulus of the corresponding  $\chi(R)$  functions with increasing temperature. c) Structure showing the spatial distribution of 1NN (4 O: blue), 2NN (6 Zn–Zn<sub>short</sub>: dark pink, 6 Zn–Zn<sub>long</sub>: light pink), and 3NN (1 Zn–O<sub>short</sub>: dark red, 9 Zn–O<sub>long</sub>: red) atoms (NN: near neighboring) atoms. d) Coordination number (CN) of Zn, Eu, 2NN (Zn+Eu), and 3NN (O) about a Zn ion; e) interatomic distances between Zn–Zn<sub>short</sub>, Zn–Zn<sub>long</sub>, Zn–Eu, Zn–O<sub>short</sub>, and Zn–O<sub>long</sub>.

synthesis temperatures would be reflected locally in the lowering of CNs, more prominently observed for higher NN than 1NN (O-shell).

The  $n_{\text{Zn-Eu}}$  values for all the ZnO:Eu nanosponges were very close to the rather low nominal value of 0.05 (Model 1). This prompted an alternative model for the Zn K EXAFS data without any contribution from Eu for comparison (Model 2). A comparative statistical parameter analysis of the two models is provided in Table S2 (Supporting Information), which reveals that the fit qualities were rather similar. This test confirmed that Eu-doping did not significantly alter the *h*-ZnO structure locally, an effect likely related to a presence of cavities in ZnO that are occupied by Eu-oxide clusters. This also explains why larger uncertainties were observed when estimating the coordination numbers and interatomic distances for the Zn–Eu pairs (Figure 2) as compared with those of Zn–Zn pairs. The largest uncertainties were observable for the 900 °C sponges in which the Zn environment contained a smaller amount of Eu. The Zn–Zn, Zn–Eu, and Zn–O interatomic distances are plotted in Figure 2e. The average Zn–Eu interatomic distances were  $\approx 0.2$  Å longer than the Zn–Zn distances, as

expected from the Eu ion's larger ionic radius of 84, 89, and 95 pm for CN = 4, 5, and 6, respectively, compared with 60 pm for tetrahedral Zn ions.<sup>[57,68]</sup> While the synthesis temperature hardly affected the Zn–Zn and short Zn–O distances of the host ZnO, the Zn–Eu and long Zn–O (3NN) distances decreased by 0.03–0.04 Å for samples made at temperatures of 700 °C and above. These observations are in concert with the XRD and TEM data, which showed an expulsion of Eu from the ZnO:Eu grains while forming *c*-Eu<sub>2</sub>O<sub>3</sub> particles on the sponge surface (Figure 1i). These changes were accompanied by a very small decrease in ZnO unit cell volume<sup>[57]</sup> during the formation of ZnO with only 30% and 50% of the Eu-oxide remaining in the ZnO grains at 900 and 800 °C, respectively (Figure 1). The mobility of the metal ions in this temperature range was also illustrated by the fast ZnO grain growth, from a size of  $\approx 10$  nm at 200–600 °C to 94 nm at 900 °C (Figure 1k). This indicates that the Eu ions form oxide clusters within ZnO, however not affecting the hosting ZnO structure to any larger degree, and that the ZnO:5%Eu is phase separated into a mixture of lower Eu content ZnO:Eu and *c*-Eu<sub>2</sub>O<sub>3</sub> at elevated temperatures.



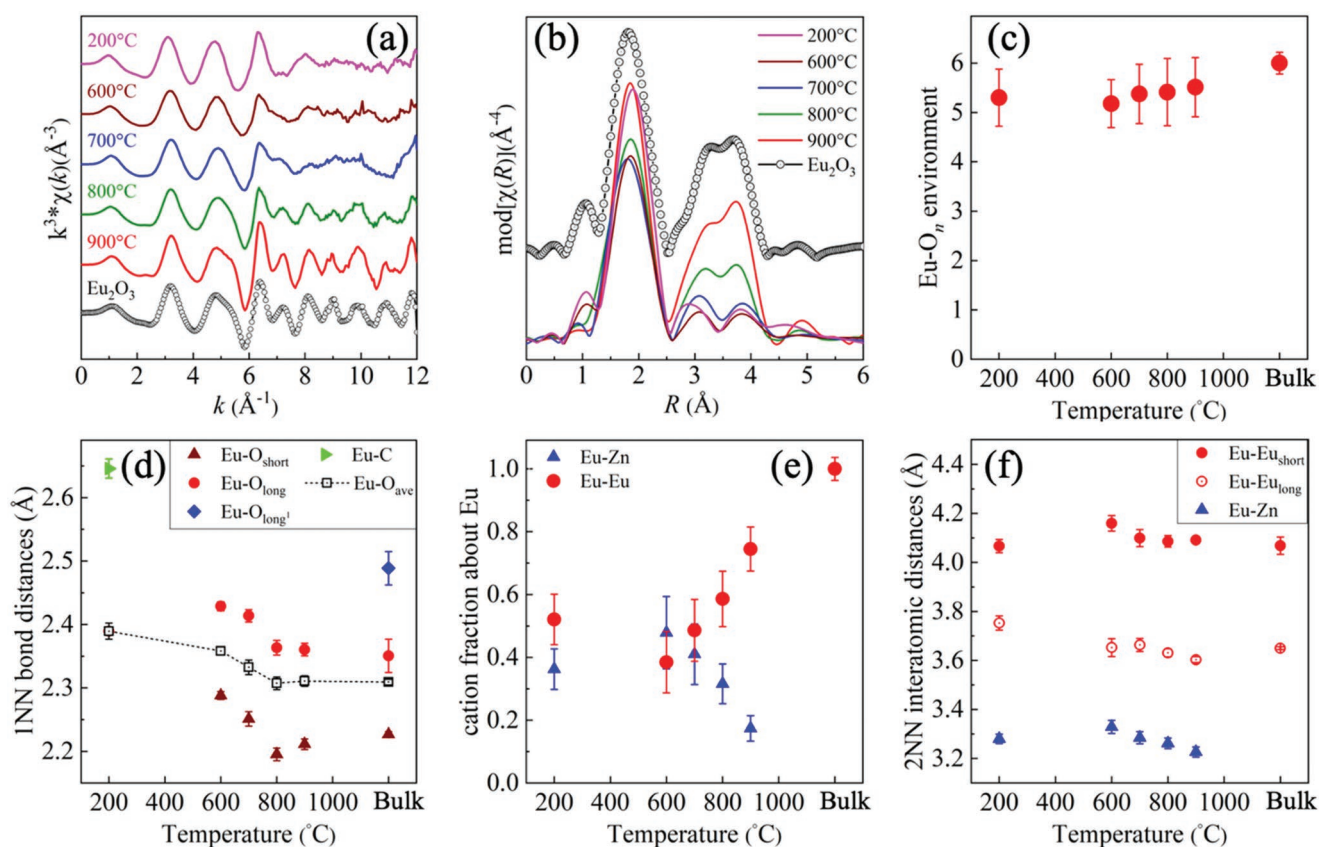


**Figure 3.** a)  $\chi(k)$  functions for Eu-doped ZnO sponges synthesized at 200, 600, 700, 800, and 900 °C and bulk *c*-Eu<sub>2</sub>O<sub>3</sub>. b) The corresponding modulus of  $\chi(R)$  functions. c) The Eu–O coordination number, CN (1NN), and d) Eu–O bond lengths (1NN). e) Fraction of Zn and Eu, respectively, about the Eu ions. f) Interatomic Eu–Eu<sub>short</sub>, Eu–Eu<sub>long</sub>, and Eu–Zn (same as Zn–Eu) distances.

### 3.2.2. Eu Environment

The local environment around the Eu ions provides experimental insight into the Eu-oxide cluster-structure within the ZnO crystals. An overlay plot of the  $\chi(k)$  functions for ZnO:5%Eu sponges, prepared at different synthesis temperatures, as well as *c*-Eu<sub>2</sub>O<sub>3</sub> for comparison, is presented in Figure 3a. The Eu L<sub>3</sub> EXAFS for the sponge prepared at 900 °C appears similar to that of *c*-Eu<sub>2</sub>O<sub>3</sub> with well-defined  $\chi(k)$  oscillations extending up to  $k_{\text{max}} \approx 11.0$  Å<sup>-1</sup>. The  $\chi(k)$  function based on the experimental data becomes slightly less well defined for the 800 °C sponge, and even more so for the lower temperatures, resulting in a  $k_{\text{max}}$  of  $\approx 8.5$  Å<sup>-1</sup>. Therefore, these results suggest a higher disorder in the local Eu environment for these samples, compared with their Zn counterpart based on  $\chi(k)$ .

The differences in Eu L<sub>3</sub>  $\chi(k)$  functions were clearly manifested in the FT of these three compounds, as shown in Figure 3b. The 1NN peaks for Eu  $\chi(R)$  appeared at larger  $R$ -values compared with the 1NN peaks for Zn  $\chi(R)$ , as expected from the ionic radius of Zn<sup>2+</sup> being smaller than Eu<sup>3+</sup>. The 1NN peaks for Eu  $\chi(R)$  were relatively broad and showed stronger intensity variations than the corresponding 1NN peaks for Zn  $\chi(R)$ , suggesting that the Eu ions assumed very varied Eu–O coordination environments. The higher NN features were rather diffuse for the synthesis temperature regime 200–700 °C but gained intensity on increasing the temperatures further.

This is interpreted as due to surface effects, interference between Eu–Zn and Eu–Eu pairs and local inhomogeneities. Increased ordering of the local Eu coordination spheres with increased synthesis temperature from 700 to 900 °C is in consonance with the formation of all six-coordinated Eu ions in crystalline *c*-Eu<sub>2</sub>O<sub>3</sub>, as concluded from XRD and TEM data.

Local structural information for Eu was obtained by fitting the EXAFS data over the range 1.1–4.2 Å. An overlay of the real part of the  $\chi(R)$  functions and their corresponding fits is presented in Figure S1b (Supporting Information). Several possibilities of host–guest interactions of the Eu ions in the ZnO structure were considered for comparison with doping models presented in the literature: metal-site substitution, interstitial doping, local clustering, and phase segregation. Further details of the EXAFS analyses, extracted local parameters and fit quality parameters for each sample at the Eu L<sub>3</sub> edge and a comparison of different models based on these parameters are provided in Table S3 (Supporting Information).

The average Eu–O CN (1NN) and Eu–O bond distances are given in Figure 3c,d, respectively. The *c*-Eu<sub>2</sub>O<sub>3</sub> structure, formed at higher temperatures, contains only CN 6 Eu ions.<sup>[68,69]</sup> The Eu ions occurring in the 200 and 600 °C samples assumed Eu CNs of  $5.3 \pm 0.6$  and  $5.2 \pm 0.5$  (Figure 3c). This is unusually low for Eu<sup>3+</sup> ions, otherwise typically attaining CN 6–8,<sup>[68]</sup> and no oxide structure possessing an Eu coordination as low as CN 5 was found in the literature. Synthesis at temperatures of 700 °C



and higher increased the Eu CN, approaching six for the 900 °C sample, in line with the formation of *c*-Eu<sub>2</sub>O<sub>3</sub>. The Eu CN of slightly lower than six, found in the 900 °C sample, is reasonable on taking into account that ≈30% of the Eu was still present in the ZnO grains, likely with a lower Eu CN than six. The extra intensity in the 1NN peak at ≈2 Å, observed for the 200 °C sample (Figure 3b), could not be accounted for by interstitial Zn or Eu doping. It might stem from organic residues, such as carboxylate groups, not fully removed at 200 °C, as identified in earlier studies using TG, XPS, and IR spectroscopy.<sup>[57]</sup>

The breadth of the 1NN peak observed in Figure 3b had to be accounted for with multiple Eu–O paths, indicating the presence of a broad range of Eu–O distances. The average Eu–O bond lengths were rather similar for the 200 and 600 °C samples measuring  $2.39 \pm 0.01$  and  $2.36 \pm 0.01$  Å, respectively, which are typical Eu–O distances in oxides. Considering that low mobility is expected in the ZnO structure at these two temperatures, 200 and 600 °C, the Eu-oxide clusters should be rather equal in size with a main difference being the presence of some organic groups, some of which are likely coordinated to the Eu ions.

Figure 3c,d shows that the number of oxygen ions around the Eu ions was larger, namely over five for all temperatures, and that metal–oxygen distances were substantially longer (≈0.4 Å) than for the ideal tetrahedral O environment around Zn in pure *h*-ZnO.<sup>[70–76]</sup> This observation rules out the possibility of Eu acting as a pure substitutional impurity. The O-shell description from EXAFS neither fits any of the possible configurations of interstitial doping, nor tetrahedral or octahedral voids, nor doping with higher Eu CN, as elaborated in the Supporting Information. Rather, it is evident that the Eu ions adopt a larger, more disordered coordination environment than the above mentioned. This finding differs from the generally proposed models for Ln-doped ZnO.

Since decoupling the effects of surface and disorder from the strongly damped  $\chi(R)$  of higher NN peaks is rather non-trivial, Figure 3e provides an estimate of the relative fraction of Zn ( $f_{\text{Eu-Zn}}$ ) and Eu ions ( $f_{\text{Eu-Eu}}$ ) instead of absolute coordination numbers of Zn ( $n_{\text{Eu-Zn}}$ ) and Eu ( $n_{\text{Eu-Eu}}$ ) surrounding an Eu ion. The reference for Eu considered here is *c*-Eu<sub>2</sub>O<sub>3</sub>, so the model of the Eu environment was achieved with a 1:1 distribution of short and long Eu–Eu correlations and one Eu–Zn correlation, as already obtained from fitting the Zn EXAFS data. If Eu ions were doped homogeneously throughout the ZnO structure, the ideal value for  $f_{\text{Eu-Eu}}$  would be 0.05, considering the nominal doping percentage of 5% Eu. But, ≈50% of the closest metal neighbors to Eu were Eu for the 200–700 °C samples (Figure 3e), which indicates that there was significant clustering of the Eu ions in the *h*-ZnO matrix. For samples made at higher temperatures this value increased up to ≈80% for the 900 °C sample, which is in concert with the extensive formation of *c*-Eu<sub>2</sub>O<sub>3</sub> at this temperature. This does not rule out that a small amount of less assembled clusters may form simultaneously within the ZnO grains. The ≈1:1 ratio of Eu–Eu and Eu–Zn pairs found for the 200–700 °C samples furthermore indicate that the clusters were small, reducing the number of Eu–O–Eu bonds (Figure 3e).

Figure 3f shows the interatomic Eu–Eu and Eu–Zn ion-pair distances. The spatial distribution of this mixed cation

substructure was found to be larger (≈0.9 Å) than its Zn analogue (≈0.6 Å), explaining why dampening effects were observed as more prominent for Eu *L*<sub>3</sub>  $\chi(R)$ , compared to Zn *K*  $\chi(R)$  (Figure 3b). The Eu–Eu distances decreased in the temperature range 700–900 °C approaching their ideal values as in bulk *c*-Eu<sub>2</sub>O<sub>3</sub>. Similar trends were observed for Zn–Eu and longer Zn–O distances in Figure 3b.

### 3.2.3. Overall Structure

The EXAFS data showed an almost unchanged *h*-ZnO structure upon doping with as high amounts as 5% EuO<sub>1.5</sub>. These findings were corroborated by XRD data that indicated a very small increase in the ZnO unit-cell volume of ≈0.4%. This is in line with a structure with small Eu-oxide clusters residing in cavities within the ZnO crystals, not easily detected with XRD and TEM. The Eu EXAFS showed unusually low Eu–oxygen coordination numbers close to five for samples heated at 200–700 °C. At higher synthesis temperatures, the CN increased toward six for the 900 °C sample, in line with the experimentally observed phase separation yielding *c*-Eu<sub>2</sub>O<sub>3</sub>. The local Eu–O coordination environment indicated a wide distribution of bond lengths in all cases. In the high temperature range, this is likely due to the presence of two phases with different average Eu CN, namely ZnO:Eu with small Eu-oxide clusters having low CN, and *c*-Eu<sub>2</sub>O<sub>3</sub>, having six-coordinated Eu. As to the samples made at lower temperature, data point toward the presence of Eu-oxide clusters with Eu ions highly disordered with varying bond lengths and unusually low Eu CN. The ≈1:1 ratio of Eu–Eu and Eu–Zn pairs, found for the 200–700 °C samples, suggests the presence of small clusters containing ≈4–8 Eu ions, assuming that they are roughly spherical. One might also consider elongated, narrow clusters to yield similar ratios of Eu–Eu and Eu–Zn pairs. This fits with the fact that no clear XRD peaks other than those of *h*-ZnO and no clusters were observed in the TEM for the 600 °C sample. For comparison, homogeneous Eu-doping was found with high-resolution STEM-high angle annular dark field (HAADF) and EELS mapping of a ZnO:1%Eu sponge synthesized at 800 °C.<sup>[58]</sup> The Eu-oxide clusters are therefore expected to be very small and aperiodic in nature, i.e., molecule-like. In contrast, heating at 700 °C and above caused phase separation of the Eu-doped ZnO sponges into *h*-ZnO with low Eu-content and *c*-Eu<sub>2</sub>O<sub>3</sub>, previously observed with XRD, TEM, and XPS studies<sup>[58]</sup> and as supported by the Eu EXAFS data showing oxygen CN around Eu nearing six.

## 3.3. DFT Modeling of the ZnO:Eu Structure

### 3.3.1. Model

A few theoretical studies on Eu-dopant structures in ZnO can be found in the literature.<sup>[74–80]</sup> Yet, to the best of our knowledge, the possibility of Eu-oxide cluster formation, as observed here, has not been considered so far. Most of these theoretically calculated structures considered single-atom doping,<sup>[74–78]</sup> isovalent doping,<sup>[79,80]</sup> or doping associated with point defects at Zn

sites (substitutional). However, the much larger ionic radius of four-coordinated  $\text{Eu}^{3+}$  ions at the  $\text{Zn}^{2+}$  position in the  $h\text{-ZnO}$  host structure makes europium ions as substitutional defects far from optimal.

To gain insight into the atomic  $\text{ZnO:5\%Eu}$  structures, a series of structures with a constant Eu-doping concentration corresponding to 4.25 mol%  $\text{EuO}_{1.5}$  (the closest approximation to nominal 5 mol%) were optimized using DFT. In this smallest structure comprising of 48 Zn ions and 48 O ions, a cluster formation implied replacing three  $\text{Zn}^{2+}$  by two  $\text{Eu}^{3+}$  and simultaneously creating one  $\text{Zn}^{2+}$  site vacancy to maintain charge neutrality. In the following, this is denoted a Eu2 cluster. In total, 23 structures were built by embedding such  $(\text{Eu}_2\text{O}_3)_x$  clusters in the ZnO structure with  $x = 1, 2$ , or 4, where the latter two were formed in supercells while keeping the Eu concentration constant. A summary of the major steps in obtaining relative total formation energies per Eu2 pair ( $\Delta E$ ) is given in Figure 4a.

### 3.3.2. Relative Formation Energy

Structure A in Figure 4a, set as reference point for comparing cluster formation energies, represents a structure with  $\text{Eu}^{3+}$  ions and accompanying  $\text{Zn}^{2+}$  vacancies randomly distributed within the ZnO structure. The first cluster structures, represented by structure B, show the effect of assembling the charges into an  $\text{Eu}^{3+}$ -dimer adjacent to a negative  $\text{Zn}^{2+}$ -vacancy, thereby forming an Eu2 cluster. This step resulted in a large energy gain ranging from 0.65 to 1.09 eV (63 to 105 kJ) per mole Eu2 cluster in ZnO. Structure C shows an example of further assembly of two Eu2 dimers into Eu4 clusters, leading to an additional energy gain of  $\approx 0.3$  eV (29 kJ) per mole Eu2 cluster in ZnO. Hence, it is not as energetically favorable as the first assembly of local positive and negative centers, but still sizeable. Further assembly into Eu8 clusters, shown in structure D, did not result in further lowering of the formation energy, but yielded similar results as the lowest

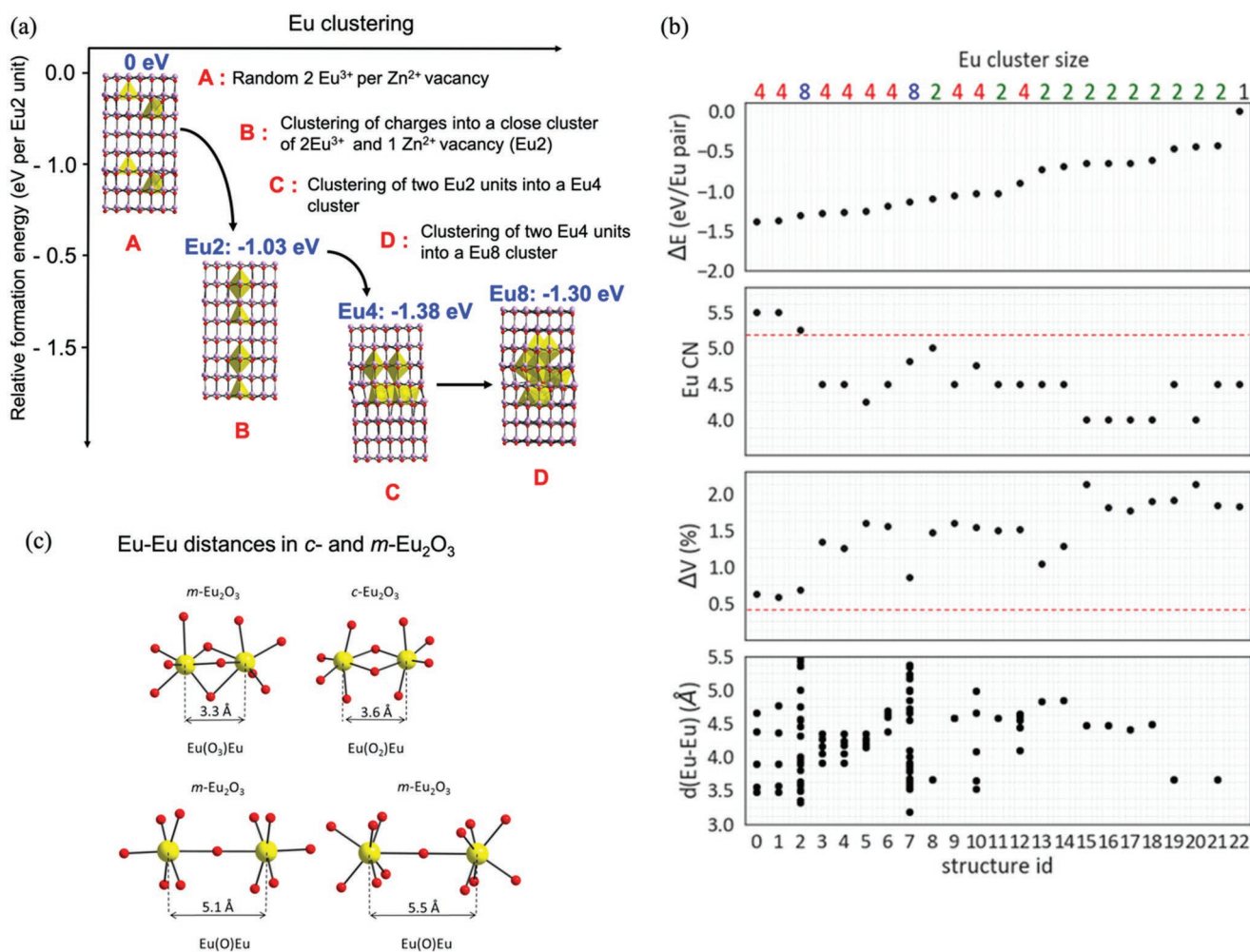


**Figure 4.** a) Theoretical  $\text{ZnO:4.25\%Eu}$  structures with europium cluster compositions based on  $(\text{Eu}_2\text{O}_3)_x$  pairs embedded in ZnO with  $x = 1, 2$ , and 4 (Eu2, Eu4, and Eu8). Yellow balls or polyhedra represent Eu ions, blue-grey balls represent Zn ions, and red balls represent O ions. b) The structures Eu2, Eu4, Eu8: numbered 2 (green), 4 (red), (blue) are ordered in total formation energy per  $\text{Eu}_2\text{O}_3$  cluster ( $\Delta E$ , eV) relative to a random ordering of 2  $\text{Eu}^{3+}$  ions and one  $\text{Zn}^{2+}$  vacancy for charge neutralization. The ZnO unit-cell volume change versus undoped ZnO ( $\Delta V_{\text{ZnO}}$  %), average Eu coordination number (CN), and Eu–Eu distances ( $d(\text{Eu-Eu})$ , Å) are also given for each structure. The red dashed line in the plots of  $\Delta V_{\text{ZnO}}$  and  $\text{CN}_{\text{Eu}}$  shows the experimental values obtained with XRD and EXAFS, respectively. c) Minimum and maximum Eu–Eu distances in c- and m- $\text{Eu}_2\text{O}_3$ .

$\Delta E$  of the Eu4 clusters. The small difference of only 0.08 eV (8 kJ) per mole Eu2 cluster in ZnO is comparable to weak hydrogen bonds.

### 3.3.3. Eu Coordination and ZnO Unit Cell Volume Relative to the Formation Energy

The findings above demonstrate a significant energy gain when forming the simplest Eu2 clusters providing local charge neutrality. However, the large ionic radius of  $\text{Eu}^{3+}$ , even at its smallest four-coordination size, should make it hard to accommodate and align with the ZnO lattice. Even if the Eu ions occupy the void of the  $\text{Zn}^{2+}$  vacancy, they may to some extent be displaced from normal site positions. Strain on the ZnO lattice reducing its stability compared to that of pure ZnO should be the consequence. As shown in Figure 4b, the lowest energy gain within the Eu2 structure (numbered as 2; green) series was obtained with four-coordinated Eu ions, yielding  $\approx 0.4$  eV higher energy relative the structures with 4.5 and 5 coordination. The latter two Eu coordination numbers were obtained when the Eu2 clusters were spatially arranged within ZnO to allow for the formation of Eu–O–Eu bonds by using the Zn vacancy. Assembling two Eu2 clusters into Eu4 clusters (numbered as 4; red) led to a gain in formation energy, where the lowest energy Eu4 clusters were obtained for those with a Eu coordination number close to 5, similar to the result for Eu2 clusters. These clusters increased their Eu coordination number by a more extensive Eu–O–Eu bonding within more tightly connected Eu-oxide clusters. This should allow for less disturbance of the hosting ZnO structure, which in its turn should lead to reduced ZnO:Eu cell volume and increased energy gain. This is also apparent from the relatively large volume expansions, typically being 1.5%–1.8% relative to undoped ZnO, for the Eu2-doped structures. This seems valid whether they had an average Eu CN of 4, 4.5, or 5, while Eu4 structures showed the largest energy gains of all, 1.4 eV/Eu-pair in relation to the reference random doping case (structure 0 and 1 in Figure 4b). These clusters also have an average Eu CN of 5.5, close to the experimental 5.2, and the lowest ZnO:Eu cell volume of the structures studied, only 0.6% larger than undoped ZnO, similar to  $\approx 0.4\%$  experimentally obtained.

Further assembly of Eu4 clusters into Eu8 clusters (numbered as 8; blue) did not significantly change the  $\Delta E$ , average Eu CN or  $\Delta V_{\text{ZnO}}$ . Similarly to the Eu2 and Eu4 clusters, a more tightly connected structure with many Eu–O–Eu bonds, yielding higher Eu CN was favorable (Structure 2), compared to a more dispersed cluster which consequently had lower Eu coordination (Structure 7).

The spherical outer orbital shell of  $\text{Eu}^{3+}$  ions allows for a wide variety of Eu–O bond lengths and spatial distribution of bonds, ultimately aiming to optimize the electronic density transfer between the metal ions and oxygens. A possible restriction for the formation of even larger cluster sizes is loss of energy gain by the Lewis acid-base interaction between the ZnO and Eu-oxide clusters, where an overall electron donation from the Eu-oxide cluster to the ZnO host is expected.

### 3.3.4. Comparison with Experimental Data

The ZnO:5%Eu sponge formed at 600 °C showed no organic or carbonate residues, nor any detectable phase separation. Therefore, it is the most intriguing and interesting to describe. The pure ZnO:4.25%Eu structures modeled by DFT should thus best describe the 600 °C sponge. As discussed above, the EXAFS data indicated an almost unchanged ZnO lattice size upon doping with the large, aliovalent  $\text{Eu}^{3+}$  ions forming small oxide clusters within the ZnO crystals. The  $\text{Eu}^{3+}$  ions in these clusters were found to have an unusually low average CN of  $5.2 \pm 0.5$ , in a wide distribution of bond lengths. As shown above, the EXAFS data agreed well with the XRD, TEM, and XPS data, which showed that the Eu-oxide clusters had to be small, nonperiodic, and not to be observed with TEM or XRD. Based on XRD, the unit-cell volume increased by  $\approx 0.4\%$  for the ZnO doped with 5%Eu compared to undoped ZnO.<sup>[57,58]</sup> It should be mentioned that for such small changes in XRD cell dimensions, the real error might in reality be large, as judged from the XRD patterns shown in previous studies.<sup>[57,58]</sup> These data mean that complementary, and in parts, unusual experimental results are present that can be used to verify the validity of theoretical DFT-based descriptions of Eu-cluster structures within the ZnO crystals. Thus, the 23 theoretical structures, including different Eu-oxide cluster structures, could be judged not only by considering their relative formation energies ( $\Delta E$ ) as described above, but also from their experimentally obtained Eu-doped ZnO unit cell volumes relative to ZnO ( $\Delta V_{\text{ZnO}}$ ), Eu–O CN ( $\text{CN}_{\text{Eu}}$ ), and Eu–Eu distances ( $d_{\text{Eu-Eu}}$ ). Furthermore, EXAFS indicated that an Eu ion should have roughly half of the closest cation neighbors being Eu ions for the 200–700 °C samples (Figure 3e). Figure 4b gives a comprehensive overview of the  $\Delta E$ ,  $\Delta V_{\text{ZnO}}$ ,  $\text{CN}_{\text{Eu}}$ , and Eu–Eu distances for the 23 theoretical structures, arranged in order of  $\Delta E$ .

### 3.3.5. Eu–Eu Distances

Examples of coordination figures from the literature showing short to long Eu–Eu distances in oxide structures are shown in Figure 4c. The  $c\text{-Eu}_2\text{O}_3$  expelled from the ZnO:Eu crystals upon heating at higher temperatures has six-coordinated  $\text{Eu}^{3+}$  ions and four-coordinated oxygens.<sup>[69]</sup> The Eu–Eu distances in this structure are close to 3.60 Å. There also exists a high temperature polymorph,  $m\text{-Eu}_2\text{O}_3$  above 1200 °C, which has a mix of six- and seven-coordinated  $\text{Eu}^{3+}$  ions and a large variety of Eu coordination geometries and Eu–Eu distances.<sup>[81]</sup> The Eu–Eu distances in this oxide range from 3.33 to 5.49 Å, with the shortest distance found between Eu ions in face-sharing  $\text{Eu}(\text{O}_3)$  Eu pairs (3.33 Å) and the longest ones for straight  $\text{Eu}(\text{O})\text{Eu}$  bonds, being 5.09 Å for CN 6 and 5.49 Å for CN 7, respectively. Another example of nearly linear (170°) Eu–O–Eu bonds with six-coordinated  $\text{Eu}^{3+}$  ions is found in the molecular Eu-oxo-alkoxide,  $\text{Eu}_5\text{O}(\text{OPr}^i)_{13}$ , with Eu–Eu distances of 4.82–4.87 Å.<sup>[82]</sup> There are also close to 90° Eu–O–Eu angles in the base plane of the square pyramidal molecule, showing very short Eu–Eu distances of 3.42–3.43 Å. These distances set the minimum and maximum Eu–Eu distances expected for CN 6 and CN 7  $\text{Eu}^{3+}$  ions in the present Eu-oxide clusters. For lower coordination



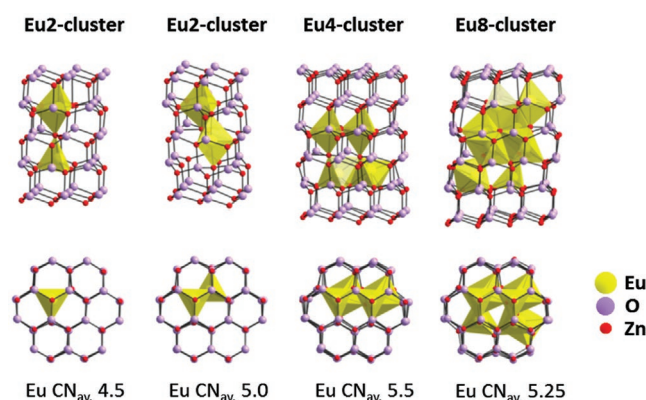


**Figure 5.** DFT-generated ZnO:4.25%Eu structures with differently sized Eu-oxide clusters as viewed from (upper row) the *a/b*-direction and (lower row) down the *c*-axis. From left to right: Eu2 cluster structures 8 and 11, Eu4 cluster structure 0, and Eu8 cluster structure 2.

numbers, somewhat shorter distances might be considered, but the  $\text{Eu}^{3+}$ – $\text{Eu}^{3+}$  electronic repulsion should make it energetically costly. The mentioned structures present Eu–O distances ranging from 2.06 to 2.49 Å, but longer distances may also be considered in the present amorphous Eu-oxide clusters.

The three clusters with the lowest  $\Delta E$  show Eu–Eu distances in the range 3.42–4.75 Å, which are reasonable distances and, moreover, fit the EXAFS data very well. These clusters, containing 4–8 Eu atoms, are also small enough to contain a large proportion of Zn–Eu pairs, as indicated by the EXAFS data. Thus, the experimental results support a doping structure similar to the three most stable clusters found by DFT. Considering the small difference in energy between these Eu4 and Eu8 clusters, and the substantial energy leap to the Eu2 clusters, it is likely that there is a distribution of cluster sizes with even numbers of Eu atoms in the range 4–8 Eu atoms. It is therefore interesting to study their structures in further detail.

### 3.3.6. Eu-Oxide Cluster Structures

As inferred from **Figure 5**, the DFT-generated Eu-oxide clusters are in all cases surrounded by an almost intact ZnO structure. The cage structures, built from ZnO tetrahedra around the Eu-oxide clusters, resemble clathrates of water and MOF inclusion compounds enclosing larger atoms or molecules in a crystalline host. However, there do occur some small distortions in the ZnO structure close to the clusters. Furthermore, the Zn ions are tetrahedrally coordinated to oxygens bonded to other Zn or Eu ions in a Eu-oxide cluster.

This indicates that once the positively charged  $\text{Eu}^{3+}$  and negatively charged  $\text{Zn}^{2+}$  vacancy centers are closely connected, the decrease in formation energy in these structures is dominated by providing the ZnO structure optimal coordination and distances. This, while having all Eu ions form at least one bond to the ZnO matrix to provide optimal conditions for electronic donation from the Lewis basic oxygens to the more Lewis acidic  $\text{Zn}^{2+}$  ions and forming as high Eu CN as possible. Structures 0 and 2, having the lowest  $\Delta E$  of the Eu4 and Eu8 clusters, are

shown together with the Eu2 structures 8 and 11 that have the lowest  $\Delta E$ . The Eu2 structures have the lowest  $\Delta E$  for clusters aligned along the ZnO *c*-axis (Structure 11), or *c* + *a/b* axis (Structure 8), yielding Eu coordination numbers of 4.5 and 5, respectively.

Eu4 and Eu8 clusters of lowest energy have similar build-ups with Eu ions coordinated by 4, 5, or 6 oxygens forming highly distorted coordination polyhedra (Figure 5). This flexibility of the Eu ions to form suitable bonds to the relatively rigid ZnO host cage, while optimizing the charge transfer between Eu ions and oxygens within the cluster, is allowed by the spherical outer orbital shell. This naturally leads to a wide range of coordination numbers and bond-lengths as reflected in the broad peaks observed in the Eu  $L_3$  EXAFS. Moreover, the clusters prefer to align along the ZnO *c*-axis and end with Eu ions oriented as a trigonal bipyramid, connecting the ZnO (0001) plane via its apex oxygen, and to the (000-1) plane, via the triangular face of a tetrahedron or octahedron. The trigonal bipyramid allows the Eu polyhedron to fit the size of the smaller ZnO tetrahedra rather well, and the trigonal faces of the octahedral or tetrahedral Eu ion similarly fit the base plane of the ZnO tetrahedra when displacing the large Eu ions towards the center of the cluster.

### 3.4. Optical Properties

The  $\text{Eu}^{3+}$  ion is well known for its excellent optical properties that can be leveraged into technological applications or be used to probe the dopant ion's local structural environment in a host lattice.<sup>[83]</sup> Therefore, the optical properties of the Eu-doped ZnO sponges were investigated by steady-state and time-resolved excitation and emission spectroscopy. ZnO:5%Eu sponges obtained at 400, 600, and 800 °C were investigated, considered as representative samples. While the 400 °C sample, that contains residual carbonate,<sup>[57]</sup> was not studied by EXAFS, it is expected to exhibit similar Eu4 to Eu8 clusters as observed by EXAFS for the other two samples. As mentioned above, the 600 °C sample is of particular interest as it is free from organic or carbonate residues, while showing no detectable phase separation into ZnO and *c*- $\text{Eu}_2\text{O}_3$ . In contrast, *c*- $\text{Eu}_2\text{O}_3$  was separated as a secondary crystalline phase in the 800 °C sample.

**Figure 6a–c** shows excitation spectra monitoring the characteristic  $\text{Eu}^{3+} {}^5\text{D}_0 \rightarrow {}^7\text{F}_2 f\text{-}f$  transition at 614 nm (in lighter colors) and the ZnO matrix emission at 545 or 550 nm (in darker colors). Irrespective of the monitored emission and synthesis temperature, the recorded excitation spectra exhibit two regions of distinct spectral features, namely below and above 375 nm. At wavelengths shorter than 375 nm, a broad band arises at  $\approx 330$  nm, the intensity of which strongly increases for the samples made at 600 and 800 °C. Photons in the UV spectral region of the observed band have an energy high enough to excite an electron from the ZnO valence band (VB) to the conduction band (CB). As to the spectral region above 375 nm, the excitation profile changed significantly between the 400 °C sample (Figure 6a) and those of the 600 and 800 °C samples (Figure 6b,c). This variance in spectral features indicates the presence of different defect states within the bandgap of ZnO (Figure 6e).<sup>[58]</sup> The sample obtained at 400 °C exhibits an excitation band at

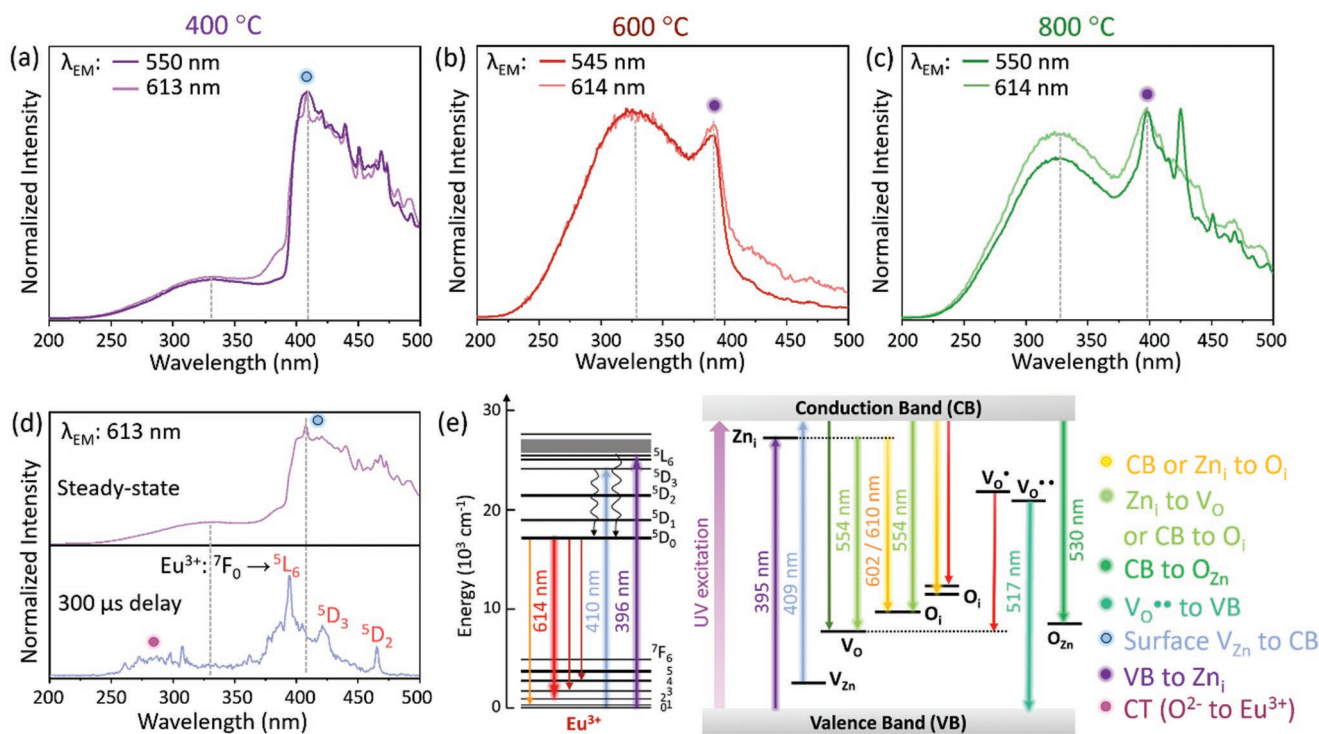


**Figure 6.** a–c) Steady-state excitation spectra of ZnO:5%Eu sponges obtained at 400, 600, and 800 °C, respectively, showing different spectral profiles stemming from various ZnO defect types. d) Bottom: time-resolved excitation spectrum of the sample obtained at 400 °C, showing  $\text{Eu}^{3+}$   $f-f$  excitation bands after a delay of 300  $\mu$ s. Top: steady-state spectrum added to highlight the contribution of ZnO excitation onto the overall spectral features. e) Energy level scheme showing the  $\text{Eu}^{3+}$  energy levels (left)<sup>[83]</sup> and ZnO defect levels (middle) in addition to valence (VB) and conduction band (CB) ( $\text{O}_{Zn}$ : anti-site oxygen atoms,  $\text{V}_{Zn}$ : zinc vacancies,  $\text{V}_O$ : oxygen vacancies,  $\text{Zn}_i$ : interstitial zinc atoms,  $\text{O}_i$ : interstitial oxygen atoms,  $\text{V}_O^{\bullet}$  and  $\text{V}_O^{\bullet\bullet}$ : singly and doubly ionized oxygen vacancies, CT: charge transfer). The attributions of the main excitation bands are given to the right.

409 nm (Figure 6a), which can be ascribed to absorption from the energy level attributed to zinc vacancies ( $\text{V}_{Zn}$ ) at the crystal surface to the ZnO conduction band (Figure 6e).<sup>[84]</sup> After excitation into the CB, radiative decay to defect states that are related to, for instance, oxygen vacancies ( $\text{V}_O$ ), interstitial oxygen atoms ( $\text{O}_i$ ), or antisite oxygen atoms ( $\text{O}_{Zn}$ ) can trigger the monitored green ZnO emission. It is noteworthy that any analogous excitation band at 409 nm was not observed for samples synthesized at 600 and 800 °C (Figure 6b,c). Instead, bands at 392 and 398 nm, likely stemming from transitions between the ZnO valence band and interstitial zinc atoms ( $\text{Zn}_i$ ), were found. Subsequent radiative decay from  $\text{Zn}_i$  to  $\text{V}_O$  defect states is one possible pathway for generating the monitored green ZnO emission. It is worth mentioning that the definite assignment of the excitation and emission (vide infra) bands resulting from different types of defects induced in the ZnO matrix is still under debate, and therefore the above attributions were suggested based on the literature and our previous spectroscopic observations for these materials.<sup>[58]</sup> Time-resolved excitation spectroscopy on the 400 °C sample was able to suppress the detection of fast ZnO related excitation bands in order to monitor the  $\text{Eu}^{3+}$  emission at 613 nm as a function of the excitation wavelength after a time delay. Figure 6d shows several  $\text{Eu}^{3+}$   $f-f$  excitation bands ascribed to the  ${}^7\text{F}_0 \rightarrow {}^5\text{L}_6$ ,  ${}^7\text{F}_0 \rightarrow {}^5\text{D}_2$ , and  ${}^7\text{F}_0 \rightarrow {}^5\text{D}_3$  transitions. The lack of the weak excitation band at  $\approx 330$  nm as well as the strong excitation band at 409 nm in the time-resolved spectrum in comparison with their presence in the steady-state

spectrum (Figure 6d) supports the suggestion that both bands are related to ZnO. Besides the peaks ascribed to  $\text{Eu}^{3+}$   $f-f$  transitions, an additional weak broad band was observed at  $\approx 280$  nm. This excitation band may be due to  $\text{Eu}^{3+} \leftarrow \text{O}^{2-}$  charge transfer (CT), where oxygen bound in the Eu-oxide clusters inside the ZnO matrix can transfer energy to  $\text{Eu}^{3+}$  ions. These broad bands observed in other Eu-based oxides have been attributed to the overall combination of charge transfer transitions in the metal–oxygen coordination sphere.<sup>[85–88]</sup>

Based on the insights gained by excitation spectroscopy, emission spectra were recorded under excitation either into the ZnO conduction band or at specific ZnO defect levels, resulting in significantly different spectral profiles for samples obtained at 400, 600, and 800 °C (Figure 7a–c). For any of the three temperatures investigated, UV excitation at  $\approx 330$  to 350 nm (darker colored curves) resulted in a broad-band emission centered in the green spectral region. Green ZnO emission is often ascribed to oxygen deficiency (i.e.,  $\text{V}_O$  or excess  $\text{Zn}^{2+}$  ions).<sup>[89]</sup> Yet, it has also been related to interstitial ( $\text{O}_i$ ) and antisite ( $\text{O}_{Zn}$ ) oxygen, having been induced upon thermal treatment of ZnO in air.<sup>[90,91]</sup> This may explain the slight blueshift of the broad emission band for the 600 and 800 °C samples, respectively, compared with the 400 °C sample under excitation into the ZnO conduction band.

The sample obtained at 400 °C (Figure 7a) exhibited an additional sharp peak at 614 nm due to the main  $\text{Eu}^{3+}$  emission ( ${}^5\text{D}_0 \rightarrow {}^7\text{F}_2$ ).<sup>[83]</sup> not present for the other samples. On changing the excitation wavelength to match the most intense excitation

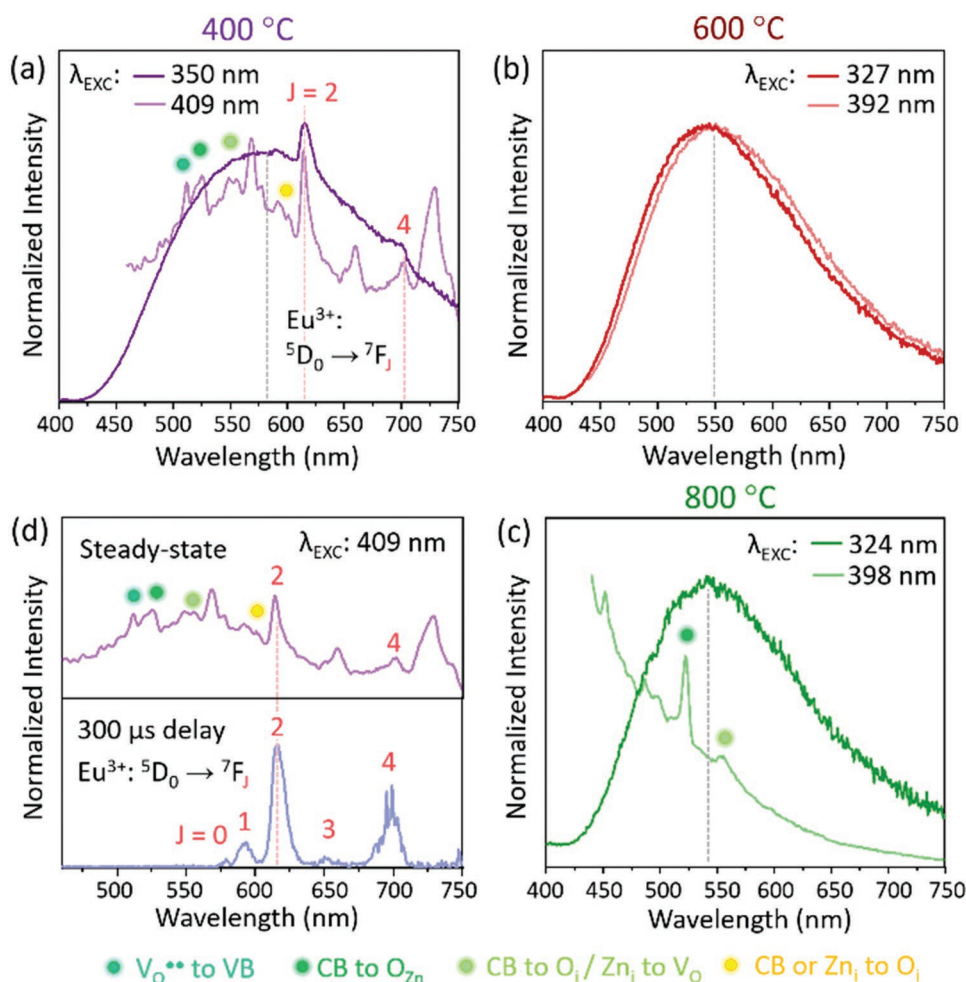


**Figure 7.** a–c) Steady-state emission spectra of ZnO:5%Eu sponges obtained at 400, 600, and 800 °C, respectively, showing different spectral profiles stemming from various ZnO defect types. d) Bottom: time-resolved emission spectrum of the sample obtained at 400 °C, showing Eu<sup>3+</sup> emission bands after a delay of 300 μs. Top: steady-state spectrum added to highlight the contribution of ZnO emission on the overall spectral features.

band for ZnO defect levels in the 400 °C sample, i.e., 409 nm (surface  $V_{\text{Zn}}$  to conduction band, lighter colored curve), sharp emission bands were observed due to ZnO defect states—including oxygen-related defect states in the 500–600 nm spectral range—in addition to the  $^5D_0 \rightarrow ^7F_2$  Eu<sup>3+</sup> emission (Figure 7a). Time-resolved spectroscopy of the Eu<sup>3+</sup> emission under 409 nm excitation (Figure 7d, bottom) further confirmed the characteristic Eu<sup>3+</sup> emission bands, whereas suppression of the ZnO emission clearly unveiled the emission bands characteristic for the Eu<sup>3+</sup>  $^5D_0 \rightarrow ^7F_J$  ( $J = 0, 1, 2, 3$ , and 4) transitions. The lack of spectral fine structure in these bands can be caused by structural disorder around the Eu<sup>3+</sup> ions,<sup>[92]</sup> induced by, for instance, carbonate residues and ZnO-related defects. Generally speaking, under UV illumination, direct excitation of the Eu<sup>3+</sup> ions into the  $^5D_1$  excited states is possible. Yet, due to the small absorption cross section of Eu<sup>3+</sup> compared to ZnO, this direct excitation pathway is most likely negligible. In addition, the radiative and nonradiative decay of excitons in ZnO is much faster ( $>10^2$  times) than the energy transfer rates to Eu<sup>3+</sup>, which hinders the direct ZnO-to-Eu<sup>3+</sup> energy transfer through the conduction band, but could lead to an emission–reabsorption mechanism.<sup>[93]</sup>

Consequently, defect states in the ZnO host are key factors to mediate energy transfer to the Eu<sup>3+</sup> levels of higher energy (e.g.,  $^5L_6$  or  $^5D_3$ ). Subsequent nonradiative decay to the emitting  $^5D_0$  level is followed by radiative decay down to the  $^7F_J$  levels giving rise to the characteristic red Eu<sup>3+</sup> emission (Figure 6e).<sup>[71,94,95]</sup>

In contrast to the 400 °C sample, the samples obtained at 600 and 800 °C—free from carbonate or other organic residues, but containing Eu-oxide clusters similar to those in the 400 °C sample and additional  $c\text{-Eu}_2\text{O}_3$  in case of 800 °C—exhibited only emission bands assigned to the ZnO matrix, regardless of the excitation wavelength used to acquire the emission spectra (Figure 7b,c). In order to ensure that the broad ZnO emission does not overlap any underlying Eu<sup>3+</sup> emission, additional time-resolved emission spectroscopy was performed on the 600 and 800 °C samples. However, no emission was observed under any of the ZnO defect- or Eu<sup>3+</sup>-related excitation wavelengths tested (namely, 330, 409, 392, 398, 464 nm—data not shown). In our previous study on Eu-doped ZnO sponges,<sup>[58]</sup> similar severe quenching of the Eu<sup>3+</sup> emission was observed for samples obtained at temperatures above 400 °C, which was attributed to two possible origins: 1) the presence of phase separation into



ZnO and *c*-Eu<sub>2</sub>O<sub>3</sub> at higher annealing temperatures inducing concentration quenching; and 2) the increased number of oxygen-related defect levels induced by heating in air at elevated temperatures, resulting in less efficient energy transfer from ZnO defect states to Eu due to the energy mismatch between these oxygen-related energy levels and the Eu<sup>3+</sup> excited levels (Figure 6e). Here, the obtained excitation spectra provide additional insight into the ZnO defect structure, not available in our previous study (Figure 6b,c). Samples annealed at 600 and 800 °C exhibited a peak at ≈395 nm, which can be ascribed to Zn<sub>i</sub> related defects in the ZnO matrix. The high energy level of this defect type provides a good energy match with the Eu<sup>3+</sup> excited states (Figure 6e), thereby potentially enabling energy transfer. Hence, possible energy transfer from ZnO to Eu<sup>3+</sup> should not be ruled out, even at higher synthesis temperatures. However, as complete lack of subsequent Eu<sup>3+</sup> emission was demonstrated by time-resolved emission spectroscopy, some quenching mechanism must be involved. In lanthanide-doped materials, photoluminescence quenching can be caused when the luminescent centers reach a critical concentration and the average distance between them is lower than a certain critical distance, known as concentration or self-quenching. For Eu<sup>3+</sup>, a critical distance of less than 5 Å is commonly considered as close enough for the exchange interaction mechanism of energy transfer to become operative.<sup>[83,96]</sup> As demonstrated by EXAFS and DFT studies, the Eu-Eu distances in the formed Eu-oxide clusters (600 °C) fall within this critical range, hence, their contribution to Eu<sup>3+</sup> luminescence quenching cannot be ruled out. Moreover, the formation of *c*-Eu<sub>2</sub>O<sub>3</sub> particles in the 800 °C sample is expected to foster non-radiative energy transfer among the luminescent Eu<sup>3+</sup> centers. While self-quenching is a plausible explanation for the observed loss of Eu<sup>3+</sup> emission, the emission spectrum of the 800 °C sample provides additional insight (Figure 7c): the two bands at 522 and 555 nm can be ascribed to a transition from the ZnO conduction band to O<sub>Zn</sub>-type defects, as well as to transitions between energy levels related to Zn<sub>i</sub> and V<sub>O</sub> defects. Specifically, the Zn<sub>i</sub> defect states are resonant with the excited Eu<sup>3+</sup> <sup>5</sup>L<sub>6</sub> level, offering a pathway for ZnO (Zn<sub>i</sub>) → Eu<sup>3+</sup> (<sup>5</sup>L<sub>6</sub>) energy transfer. However, as no Eu<sup>3+</sup> emission was detected, such energy transfer may compete with the ZnO matrix-related radiative decay. If the latter is favored, ZnO-to-Eu energy transfer would be hampered, which ultimately can explain the observation of green ZnO emission only.

Overall, the observed excitation and emission spectra of ZnO:5%Eu obtained at different temperatures show how the optical properties in ZnO:5%Eu sponges are strongly dictated by changes in the local host structure as well as the dopant ion environment and its interaction with the local host structure. Loss of Eu<sup>3+</sup> photoluminescence in samples formed at 800 °C was attributed to commonly observed concentration quenching due to secondary *c*-Eu<sub>2</sub>O<sub>3</sub> phase formation as well as changes in the ZnO defect structure. Most interestingly, complementary EXAFS and DFT analysis provided a possible explanation for the lack of Eu<sup>3+</sup> photoluminescence in samples annealed at lower temperature (600 °C). These samples did not suffer from phase separation, while the ZnO defect structure might be suitable for energy transfer to Eu<sup>3+</sup>, thus, photoluminescence was expected. The lack of the expected emission can likely be explained by the existence of Eu clusters with short Eu–Eu distances in these

nanosponges, as unveiled by EXAFS and DFT analysis in addition to XRD and TEM techniques. It is interesting to note that seemingly homogeneously doped samples, as based on XRD and TEM analysis, may exhibit molecule-like dopant clusters. These in turn, can result in optical properties that differ from those expected for homogeneously dispersed dopants.

## 4. Conclusions

This study provides a possible explanation how high concentrations of large, aliovalent Eu<sup>3+</sup> ions can be introduced into the ZnO structure without forming detectable extra phases and causing virtually no increase in the host ZnO unit-cell volume. This might also be extended to other Ln<sup>3+</sup> ions in light of their similarities in formation of various oxide structures, owing to their spherical outer shell not favoring directional bonds and ionic radius differences of only about 1 pm per element number. For the pure oxide ZnO:5%Eu sponges obtained at 600 °C without any phase separation, the ZnO unit-cell volume expansion was quite small compared to the undoped ZnO, in spite of the large, aliovalent Eu<sup>3+</sup> ions present in ZnO. The Zn edge EXAFS results fitted the XRD studies well and showed a low average Eu-ion coordination number of ≈5.2 for this sample. DFT calculations of Eu-doped ZnO structures yielded the lowest relative formation energy for three clusters, embedded in the ZnO structure, formed by four or eight Eu atoms. These clusters showed Eu coordination numbers of 5.2–5.5, reasonable Eu–Eu distances, and only ≈0.6% ZnO:Eu unit-cell volume expansion compared to undoped ZnO. These numbers are judged to be within the error of the experimentally obtained values which indicates that these hypothetical structures, built from an almost unchanged ZnO host with inclusions of molecule-like nonperiodic Eu<sub>4</sub>O<sub>6</sub> to Eu<sub>8</sub>O<sub>12</sub> clusters, are likely close to the real structures. Smaller Eu clusters of two Eu<sup>3+</sup> ions accompanied by a Zn<sup>2+</sup> vacancy were higher in energy, showed much larger ZnO:5%Eu volume expansion compared with ZnO, and deviated from the experimental results in several ways. The ZnO:5%Eu nanocrystalline sponges showed that a phase separation into ZnO with a lower amount of Eu-doping and *c*-Eu<sub>2</sub>O<sub>3</sub> took place at synthesis temperatures of 700 °C and higher. A comparative study of excitation and emission spectra of ZnO:5%Eu obtained at different temperatures revealed how such unique dopant environments at a given temperature influence the optical properties of these oxide nanosponges. These findings may provide insights that provide support in a more rational design of next-generation magnetic and optic semiconductor materials based on embedded metal oxide clusters.

## Supporting Information

Supporting Information is available from the Wiley Online Library or from the author.

## Acknowledgements

MRCAT operations were supported by the Department of Energy and the MRCAT member institutions. This research used resources of the

Advanced Photon Source, a U.S. Department of Energy (DOE) Office of Science User Facility operated for the DOE Office of Science by Argonne National Laboratory Swedish Energy Agency under Contract No. DE-AC02-06CH11357. The authors also acknowledge STandUP for Energy, the National strategic e-science program eSSSENCE, the Swedish Research Council (Grant Nos. VR 2017-04341, 2018-06465, and 2018-04330), the Swedish Foundation for Strategic Research (Project No. RMA15-0130), and the Swedish Energy Agency (Grant No. P43549-1) for financial support. G.W. gratefully acknowledges financial support from the O. E. Nycander Foundation. E.H. and E.M.R. gratefully acknowledge the financial support provided by the University of Ottawa, the Canadian Foundation for Innovation (CFI), and the Natural Sciences and Engineering Research Council of Canada (NSERC). The simulations were performed on resources provided by the Swedish National Infrastructure for Computing (SNIC) (Grant Nos. 2020/1-41 and 2021/1-32) at HPC2N, and NSC.

## Conflict of Interest

The authors declare no conflict of interest.

## Data Availability Statement

The data that support the findings of this study are available from the corresponding author upon reasonable request.

## Keywords

density functional theory (DFT), dopant structures, doped ZnO, extended X-ray absorption fine structure (EXAFS), lanthanide doping, solution processing, sponges

Received: May 29, 2022

Revised: October 14, 2022

Published online: November 20, 2022

- [1] Ü. Özgür, Ya. I. Alivov, C. Liu, A. Teke, M. A. Reshchikov, S. Doğan, V. Avrutin, S.-J. Cho, H. A. Morkoç, *J. Appl. Phys.* **2005**, *98*, 041301.
- [2] A. Kołodziejczak-Radzimska, T. Jesionowski, *Materials* **2014**, *7*, 2833.
- [3] Z. L. Wang, *J. Phys. Condens. Matter* **2004**, *16*, R829.
- [4] B. I. Kharisov, O. V. Kharissova, B. O. García, Y. P. Méndez, I. Gómez de la Fuente, *RSC Adv.* **2015**, *5*, 105507.
- [5] V. Cauda, D. Pugliese, N. Garino, A. Sacco, S. Bianco, F. Bella, A. Lamberti, C. Gerbaldi, *Energy* **2014**, *65*, 639.
- [6] E. Hosono, S. Fujihara, I. Honma, H. Zhou, *Adv. Mater.* **2005**, *17*, 2091.
- [7] M. Law, L. E. Greene, J. C. Johnson, R. Saykally, P. Yang, *Nat. Mater.* **2005**, *4*, 455.
- [8] J. A. Anta, E. Guillén, R. Tena-Zaera, *J. Phys. Chem. C* **2012**, *116*, 11413.
- [9] I. Gonzalez-Valls, M. Lira-Cantu, *Energy Environ. Sci.* **2009**, *2*, 19.
- [10] G. S. Selopal, H.-P. Wu, J. Lu, Y.-C. Chang, M. Wang, A. Vomiero, I. Concina, E. Diau, E. W.-G. Diau, *Sci. Rep.* **2016**, *6*, 18756.
- [11] F. Zhao, J. Lin, Z. Lei, Z. Yi, F. Qin, J. Zhang, L. Liu, X. Wu, W. Yange, P. Wu, *Phys. Chem. Chem. Phys.* **2022**, *24*, 4871.
- [12] Y. Zhang, M. K. Ram, E. K. Stefanakos, D. Y. Goswami, *J. Nanomater.* **2012**, *2012*, 624520.
- [13] S. G. Kumar, R. Kavitha, *Sep. Purif. Technol.* **2021**, *274*, 118853.
- [14] K. M. Lee, C. W. Lai, K. S. Ngai, J. C. Juan, *Water Res.* **2016**, *88*, 428.
- [15] R. Boppella, K. Anjaneyulu, P. Basak, S. V. Manorama, *J. Phys. Chem. C* **2013**, *117*, 4597.
- [16] Z. Mirzaeifar, Z. Shariati, M. Jourshabani, S. Mahmood, R. Darvishi, *Ind. Eng. Chem. Res.* **2020**, *59*, 15894.
- [17] C. Liu, F. Yun, H. Morkoç, *J. Mater. Sci.* **2005**, *16*, 555.
- [18] S. J. Pearton, W. H. Heo, M. Ivill, D. P. Norton, T. Steiner, *Semicond. Sci. Technol.* **2004**, *19*, R59.
- [19] K. R. Kittilstved, W. K. Liu, D. R. Gamelin, *Nat. Mater.* **2006**, *5*, 291.
- [20] M. M. Obeid, H. R. Jappor, K. Al-Marzoki, I. Ali Al-Hydary, S. J. Edrees, M. M. Shukur, *RSC Adv.* **2019**, *9*, 33207.
- [21] M. Willander, O. Nur, Q. X. Zhao, L. L. Yang, M. Lorenz, B. Q. Cao, J. Z. Pérez, C. Czekalla, G. Zimmermann, M. Grundmann, *Nanotechnology* **2009**, *20*, 332001.
- [22] L. Shi, J. Cui, F. Zhao, D. Wang, T. Xie, Y. Lin, *Phys. Chem. Chem. Phys.* **2015**, *17*, 31316.
- [23] W. G. Hoffmann, A. E. Gad, J. D. Prades, F. Hernandez-Ramirez, R. Fiz, H. Shen, S. Mathur, *Nano Energy* **2013**, *2*, 514.
- [24] K. J. Choi, H. W. Jang, *Sensors* **2010**, *10*, 4083.
- [25] J. Zhang, S. Wang, M. Xu, Y. Wan, B. Zhu, S. Zhang, W. Huang, S. Wu, *Cryst. Growth Des.* **2009**, *9*, 3532.
- [26] V. Postica, A. Vahl, D. Santos-Carballal, T. Dankwort, L. Kienle, M. Hoppe, A. Cadi-Essadek, N. H. de Leeuw, M.-I. Terasa, R. Adelung, F. Faupel, O. Lupan, *ACS Appl. Mater. Interfaces* **2019**, *11*, 31452.
- [27] M. P. Pratik, M. P. Vikas Patel, C. K. Sumesh, D. J. Late, *Sol. Energy* **2020**, *206*, 974.
- [28] M. Behrens, R. Schlögl, *Z. Anorg. Allg. Chem.* **2013**, *639*, 2683.
- [29] M. Hosseini-Sarvari, *Curr. Org. Synth.* **2013**, *10*, 697.
- [30] L. Martínez-Suárez, N. Siemer, J. Frenzel, D. Marx, *ACS Catal.* **2015**, *5*, 4201.
- [31] V. Polshettiwar, B. Baruwati, R. S. Varma, *ACS Nano* **2009**, *3*, 728.
- [32] M. Behrens, F. S. Kasatkin, S. K. M. Hävecker, F. Abild-Pedersen, S. Zander, F. Girgsdies, P. Kurr, B.-L. Kniep, M. Tovar, R. W. Fischer, J. K. Nørskov, R. Schlögl, *Science* **2012**, *336*, 893.
- [33] G. Pradhan, Y. C. Sharma, *Fuel* **2021**, *284*, 118966.
- [34] V. Caramia, B. Bozzini, *Mater. Renewable Sustainable Energy* **2014**, *3*, 28.
- [35] J. F. Parker, E. S. Nelson, M. D. Wattendorf, C. N. Hevrin, J. W. Long, D. R. Rolison, *Appl. Mater. Interfaces* **2014**, *6*, 19471.
- [36] N. Garino, A. Lamberti, R. Gazia, A. Chiodoni, C. Gerbaldi, *J. Alloys Compd.* **2014**, *15*, S454.
- [37] F. Wen, C. Zhu, L. Li, B. Zhou, L. Zhang, C. Han, W. Li, Z. Yue, W. Wu, G. Wang, S. Zhang, *Chem. Eng. J.* **2022**, *430*, 132676.
- [38] S. Mukherjee, D. Phuyal, C. U. Segre, S. Das, O. Karis, T. Edvinsson, H. Rensmo, *Phys. Chem. C* **2021**, *125*, 14910.
- [39] H. Ganegoda, S. Mukherjee, B. Ma, D. T. Olive, J. H. McNeely, J. A. Kaduk, J. Terry, H. Rensmo, C. U. Segre, *J. Phys. Chem.* **2021**, *125*, 12342.
- [40] S. Mukherjee, H. Ganegoda, A. Kumar, S. Pal, C. U. Segre, D. D. Sarma, *Inorg. Chem.* **2018**, *57*, 9012.
- [41] A. H. Khan, A. Dalui, S. Mukherjee, C. U. Segre, D. D. Sarma, S. Acharya, *Angew. Chem., Int. Ed.* **2015**, *54*, 2643.
- [42] T. Dietl, H. Ohno, J. Cibert, D. Ferrand, *Science* **2000**, *287*, 1019.
- [43] S.-Y. Seo, E.-S. Jeong, C.-H. Kwak, C.-I. Park, Z. Jin, S.-H. Kim, S.-W. Han, *J. Phys. Condens. Matter* **2013**, *25*, 256005.
- [44] M. A. White, S. T. Ochsenein, D. R. Gamelin, *Chem. Mater.* **2008**, *20*, 7107.
- [45] S. Ramachandran, A. Tiwari, J. Narayan, *J. Appl. Phys. Lett.* **2004**, *84*, 5255.
- [46] A. K. Yadav, S. Maidul Haque, D. Shukla, D. M. Phase, S. N. Jha, D. Bhattacharyya, *J. Appl. Phys.* **2012**, *112*, 043513.
- [47] S. Mal, S. Nori, S. Mula, J. Narayan, J. T. Prater, *J. Appl. Phys.* **2012**, *112*, 113917.
- [48] M. A. White, T. C. Lovejoy, S. T. Ochsenein, M. A. Olmstead, D. R. Gamelin, *J. Appl. Phys.* **2010**, *107*, 103917.

- [49] C. I. Park, Z. Jin, E.-S. Jeong, I. H. Hwang, S. W. Han, *J. Korean Phys. Soc.* **2013**, 63, 2165.
- [50] B. Sanyal, O. Grånäs, R. Knut, V. A. Coleman, P. Thunström, D. M. Iușan, O. Karis, O. Eriksson, G. Westin, *J. Appl. Phys.* **2008**, 103, 07D130.
- [51] D. Iușan, R. Knut, B. Sanyal, O. Karis, O. Eriksson, V. A. Coleman, G. Westin, J. M. Wikberg, P. Svedlindh, *Phys. Rev.* **2008**, B 78, 085319.
- [52] R. Knut, J. M. Wikberg, K. Lashgari, V. A. Coleman, G. Westin, P. Svedlindh, O. Karis, *Phys. Rev. B* **2010**, 82, 094438.
- [53] C. X. Kronawitter, I. Zegkinoglou, S.-H. Shen, P. Liao, I. S. Cho, O. Zandi, Y.-S. Liu, K. Lashgari, G. Westin, J.-H. Guo, F. J. Himpsel, E. A. Carter, X. L. Zheng, T. W. Hamann, B. E. Koel, S. S. Mao, L. Vayssieres, *Energy Environ. Sci.* **2014**, 7, 3100.
- [54] R. Marin, D. Jaque, *Chem. Rev.* **2021**, 121, 1425.
- [55] V. Kumar, O. M. Ntwaebrowa, T. Soga, V. Dutta, H. C. Swart, *Photonics* **2017**, 4, 2613.
- [56] S. G. Kumar, R. Kavitha, *Sep. Purif. Technol.* **2021**, 274, 118853.
- [57] S. Naim Katea, P. Broqvist, J. Kullgren, E. Hemmer, G. Westin, *Inorg. Chem.* **2020**, 59, 7584.
- [58] R. Marin, F. Oussta, S. Naim Katea, S. Prabhudev, G. A. Botton, G. Westin, E. Hemmer, *J. Mater. Chem.* **2019**, 7, 3909.
- [59] J. P. Perdew, K. Burke, M. Ernzerhof, *Phys. Rev. Lett.* **1996**, 77, 3865.
- [60] J. P. Perdew, K. Burke, M. Ernzerhof, *Phys. Rev. Lett.* **1996**, 78, 1396.
- [61] G. Kresse, J. Hafner, *Phys. Rev. B* **1993**, 47, 558.
- [62] G. Kresse, J. Hafner, *Phys. Rev. B* **1994**, 49, 14251.
- [63] G. Kresse, F. Furthmüller, *Comput. Mater. Sci.* **1996**, 6(1), 15.
- [64] G. Kresse, F. Furthmüller, *Phys. Rev. B* **1996**, 54, 11169.
- [65] P. E. Blöchl, *Phys. Rev. B* **1994**, 50, 17953.
- [66] G. Kresse, D. Joubert, *Phys. Rev. B* **1999**, 59, 1758.
- [67] S. N. Katea, Š. Hajduk, Z. C. Orel, G. Westin, *Inorg. Chem.* **2017**, 56, 15150.
- [68] R. D. Shannon, *Acta Crystallogr.* **1976**, A32, 751.
- [69] PDF Card–00-034-0392.
- [70] Y. Zhang, Y. Liu, L. Wu, E. Xie, J. Chen, *J. Phys. D: Appl. Phys.* **2009**, 42, 085106.
- [71] S. M. Ahmed, P. Szymanski, L. M. El-Nadi, M. A. El-Sayed, *ACS Appl. Mater. Interfaces* **2014**, 6, 1765.
- [72] Y. H. Yang, Y. Feng, H. G. Zhu, G. W. Yang, *J. Appl. Phys.* **2010**, 107, 053502.
- [73] W.-W. Zhong, G.-W. Guan, X.-L. Liu, Li. Zhang, Y.-P. Liu, Z.-G. Li, W.-P. Chen, *J. Nanomater.* **2012**, 2012, 263679.
- [74] S. Geburt, M. Lorke, A. L. da Rosa, T. Frauenheim, R. Röder, T. Voss, U. Kaiser, W. Heimbrot, C. Ronning, *Nano Lett.* **2014**, 14, 4523.
- [75] M. H. N. Assadi, Y. Zhang, R.-K. Zheng, S. P. Ringer, S. Li, *Nanoscale Res. Lett.* **2011**, 6, 357.
- [76] A. G. El Hachimi, M. L. Ould NE, A. El Yousfi, A. Benyoussef, A. El Kenz, *J. Rare Earths* **2019**, 37, 416.
- [77] M. Lorke, T. Frauenheim, A. L. da Rosa, *Phys. Rev.* **2016**, B93, 115132.
- [78] X. J. Zhang, W. B. Mi, X. C. Wang, H. L. Bai, *J. Alloys Compd.* **2014**, 617, 828.
- [79] A. Yumak, U. Yahsi, P. Petkova, K. Boubake, *Mater. Lett.* **2016**, 164, 89.
- [80] Q. Yu, T. Ai, L. Jiang, Y. Zhang, C. Lia, X. Yuan, *RSC Adv.* **2014**, 4, 53946.
- [81] PDF Card–00-034-00721.
- [82] G. Westin, M. Moustiakimov, M. Kritikos, *Inorg. Chem.* **2002**, 41, 3249.
- [83] K. Binnemans, *Coord. Chem. Rev.* **2015**, 295, 1.
- [84] D. Chen, Z. Wang, T. Ren, H. Ding, W. Yao, R. Zong, Y. Zhu, *J. Phys. Chem. C* **2014**, 118, 15300.
- [85] W. Ran, H. M. Noh, S. H. Park, B. K. Moon, J. H. Jeong, J. H. Kim, J. Shi, *Sci. Rep.* **2018**, 8, 5936.
- [86] L. Yang, Y. She, S. Zhao, S. Yue, Q. Wang, A. Hu, W. Zhang, *J. Appl. Phys.* **2010**, 108, 104301.
- [87] G. Wakefield, H. A. Keron, P. J. Dobson, J. H. Hutchison, *J. Colloid Interface Sci.* **1999**, 215, 179.
- [88] I. P. Roof, M. D. Smith, S. Park, H.-C. zur Loye, *J. Am. Chem. Soc.* **2009**, 131, 4202.
- [89] Y. Zheng, C. Chen, Y. Zhan, X. Lin, Q. Zheng, K. Wei, J. Zhu, Y. Zhu, *Inorg. Chem.* **2007**, 46, 6675.
- [90] M. M. Can, S. I. Shah, M. F. Doty, C. R. Haughn, T. Firat, *J. Phys. D: Appl. Phys.* **2012**, 45, 195104.
- [91] R. Raji, K. G. Gopchandran, *J. Sci.: Adv. Mater. Devices* **2017**, 2, 51.
- [92] K. W. Jang, R. S. Meltzer, *Phys. Rev. B* **1995**, 52, 6431.
- [93] Y.-P. Du, Y.-W. Zhang, L.-D. Sun, C.-H. Yan, *J. Phys. Chem.* **2008**, 112, 12234.
- [94] S. Ghosh, K. U. M. Kumar, B. N. S. Bhaktha, *Opt. Mater.* **2017**, 64, 288.
- [95] S. Senapati, K. K. Nanda, *J. Mater. Chem. C* **2017**, 5, 1074.
- [96] V. Mangalam, K. Pita, *Opt. Mater. Express* **2018**, 8, 3115.